X chromosome encoded histone demethylase UTX regulates mammalian axon regeneration via microRNA-124

Shu-Guang Yang[1, 2, #], Xue-Wei Wang[2, #], Chang-Ping Li[4, #], Tao Huang[5, #], Qiao Li[2], Ling-Rui Zhao[2], Cheng Qian[2], Saijilafu[6], Chang-Mei Liu[4, *], and Feng-Quan Zhou[2, 3, 1, *]

[1] Sir Run Run Shaw Hospital, Zhejiang University School of Medicine, Hangzhou, Zhejiang 310016, China

[2] Department of Orthopedic Surgery, The Johns Hopkins University School of Medicine, Baltimore, MD 21205, USA

[3] The Solomon H. Department of Neuroscience, The Johns Hopkins University School of Medicine, Baltimore, MD 21205, USA

[4] State Key Laboratory of Stem Cell and Reproductive Biology, Institute of Zoology, Chinese Academy of Sciences; University of Chinese Academy of Sciences; Beijing Institute for Stem Cell and Regenerative Medicine, Beijing 100101, China.

[5] State Key Laboratory of Frigid Zone Cardiovascular Diseases (SKLFZCD), Department of Cardiovascular Surgery, General Hospital of Northern Theater Command, Shenyang, Liaoning 110016, China.

[6] Key Laboratory of Novel Targets and Drug Study for Neural Repair of Zhejiang Province, School of Medicine, Hangzhou City University, Hangzhou, Zhejiang 310015, China

[#] These authors contributed equally to this study

*Correspondence:
Chang-Mei Liu, Ph.D. Email: liuchm@ioz.ac.cn
Feng-Quan Zhou, Ph.D. Email: fzhou4@zju.edu.cn

Running head: Regulation of axon regeneration by histone methylation

SUMMARY

Neurons in the mammalian central nervous system (CNS) gradually lose their intrinsic regeneration capacity during maturation mainly because of altered transcription profile. Recent studies have made great progress by identifying genes that can be manipulated to enhance CNS regeneration. However, as a complex process involving many genes and signaling networks, it is of great importance to deciphering the underlying neuronal chromatin and transcriptomic landscape coordinating CNS regeneration. Here we identify UTX, an X-chromosome associated gene encoding a histone demethylase, as a novel regulator of mammalian neural regeneration. We demonstrate that UTX acts as a repressor of spontaneous axon regeneration in the peripheral nerve system (PNS). In the CNS, either knocking out or pharmacological inhibiting UTX in retinal ganglion cells (RGCs) leads to significantly enhanced neuronal survival and optic nerve regeneration. RNA-seq profiling revealed that deleting UTX switches the RGC transcriptomics into a developmental-like state. Moreover, microRNA-124, one of the most abundant microRNAs in mature neurons, is identified as a downstream target of UTX and blocking endogenous microRNA124-5p results in robust optic nerve regeneration. These findings revealed a novel histone modification-microRNA epigenetic signaling network orchestrating transcriptomic landscape supporting CNS neural regeneration.

KEYWORDS

UTX, histone methylation, H3K27me3, microRNA-124, glaucoma, axon regeneration, optic nerve regeneration, chromatin structure

50 **INTRODUCTION**

51 Axon regeneration in the mammalian central nervous system (CNS) has been a long standing
52 and highly challenging issue in the biomedical research field. A major reason for the failed CNS axon
53 regeneration is that mature mammalian CNS neurons permanently lose their intrinsic ability to support
54 axon growth during maturation.[1-3] Recent studies have identified many genes that could be
55 manipulated to significantly boost the intrinsic axon regeneration ability of mature CNS neurons,
56 including *PTEN*, *KLF4/6/7/9*, *GSK3β*, *SOCS3*, *c-MYC*, *B-RAF, and Lin28*.[4-12] However, the molecular
57 mechanisms, especially at the transcriptional and chromatin regulation level, by which many genes act
58 coordinately to regulate axon regeneration is still rudimentary and fragmented. Thus, understanding
59 the intrinsic transcriptomic networks and chromatin modulation specifically underlying axon growth
60 during development and regeneration is of great importance in the neural regeneration field.

61 Epigenetic regulation is a key mechanism to control chromatin structure and the subsequent
62 transcriptomic state[13], making it a likely mechanism for regulating the intrinsic axon regeneration
63 ability. There are three major epigenetic modifications, including DNA methylation, histone
64 modification, and non-coding RNAs. Epigenetic regulation of gene expression has been widely studied
65 in many other fields, such as cancer and stem cells. To date there is emerging evidence that epigenetic
66 regulation also plays key roles in controlling neural regeneration, although most of which were related
67 to spontaneously occurred PNS regeneration. For instance, several studies, including ours,[11, 14-19] have
68 illustrated the important roles of microRNAs in regulation of PNS axon regeneration. In addition, DNA
69 methylation has also been shown to be involved in axon regeneration.[20-22] Dynamic histone acetylation
70 could control chromatin accessibility and gene transcription of regeneration-associated genes (RAGs)
71 to enable the regenerative capacity.[23-26] Moreover, our study[16] has provided *in vivo* evidence that

microRNA-138 and histone deacetylase SIRT1 form a mutual negative feedback loop to control sensory axon regeneration, suggesting crosstalk between two epigenetic signaling. Furthermore, a recent study[27] using multiomics sequencing characterized the unique chromatin signature and associated transcription profile during spontaneous sensory axon regeneration, highlighting the key roles of histone acetylation in supporting axon regeneration.

Ubiquitously transcribed X chromosome tetratricopeptide repeat protein (*UTX*, also named *KDM6A*) and Jumonji domain-containing protein 3 (*JMJD3*, also named *KDM6B*) are chromatin modifiers that specifically erase trimethyl groups of H3 histone at lysine 27 (H3K27me3), thereby generating transcriptionally permissive chromatin.[28, 29] The roles and mechanisms of both UTX and JMJD3 have been extensively studied for their involvement in development[28-30], differentiation[31, 32], cell plasticity[33], aging[34-37], cell reprogramming[38, 39], inflammatory response[40, 41], tumorigenesis[42, 43], and neurodegeneration[44, 45]. In the nervous system, our recent studies[46] demonstrated that UTX functioned to regulate neuronal dendritic development and various cognitive functions through demethylation of H3K27me3. In addition, previous studies suggested that JMJD3 served as a crucial regulator of neuronal maturation and survival.[47, 48] In contrast, our latest study[49] revealed that H3K27 methyltransferase EZH2 acts to control multiple steps of neuronal morphogenesis during development, thereby leading to cognitive consequences in adult mice. There is early evidence that PNS axotomy can trigger dynamic changes of histone methylation in sensory neurons.[26] However, to date, the functional role of histone methylation in axon regeneration is still under intensive investigation.

Here, we report that deleting *UTX* or *JMJD*3 significantly promotes sensory axon regeneration *in vivo*. Importantly, deleting *UTX* in retinal ganglion cells (RGCs) markedly enhanced optic nerve regeneration. Mechanistically, our data demonstrated that UTX acted via a PTEN/PI3K independent

94 pathway to enhance optic nerve regeneration. Moreover, by analyzing and comparing transcriptomic
95 changes of purified RGCs during development/maturation to that of *UTX* knockout, we found that
96 deleting *UTX* reactivated developmental-like growth programs via modified chromatin structure and
97 transcriptomics in RGCs. Finally, RNA sequencing analysis identified miR-124-5p as a downstream
98 target of *UTX* to regulate optic nerve regeneration, and inhibiting miR-124-5p directly was sufficient
99 to enhance long distance optic nerve regeneration. Collectively, our findings revealed that X
100 chromosome encoded histone demethylase, together with its downstream target miR-124-5p, formed
101 an epigenetic network to regulate mammalian neural regeneration by reshaping the neuronal
102 transcriptomic landscape to a developmental-like state.

RESULTS

UTX and JMJD3 are negative regulators of spontaneous sensory axon regeneration

To characterize the roles of demethylases UTX and JMJD3 in axon injury and regeneration, we first examined how they acted in sensory neurons in the dorsal root ganglion (DRG) during spontaneous axon regeneration. We performed immunostaining analyses to examine how sciatic nerve injury (SNI) affected the protein levels of UTX or JMJD3 in sensory neurons *in vivo*. The results showed that the protein levels of UTX in the nuclei of sensory neurons were significantly reduced 1- and 3-days post SNI *in vivo* (Fig. 1a, b). JMJD3 staining demonstrated that it was presented in both cytoplasm and the nucleus in uninjured naïve neurons, but gradually excluded from the nucleus after SNI (Fig. 1c, d). Time-course analyses by real time PCR further showed that the mRNA levels of *UTX* were gradually downregulated after SNI, reaching its minimum at day 7 post-SNI (Fig. 1e). Similarly, the levels of *JMJD3* were also significantly reduced 1 day post-SNI but recovered back at day 7 (Fig. 1e). As a result, the level of H3K27me3 was significantly increased after SNI.[50] Together, these data suggested that histone demethylases UTX and JMJD3 might function to suppress axon regeneration. To test this idea, we used our well-established *in vivo* electroporation technique [51] to co-transfect sensory neurons with a group of 4 different siRNAs against *UTX* or *JMJD3* and the EGFP plasmid. According to our previous study, the transfection efficiency of fluorescence labeled siRNAs and EGFP via *in vivo* electroporation is over 96%[11], and 5-10%[51], respectively. Therefore, we considered all EGFP positive neurons as siRNA positive. Western blot results showed that siRNAs significantly reduced the protein levels of UTX or JMJD3 *in vivo* (Fig. 1f, g). To assess functionally how down-regulation of UTX or JMJD3 affected sensory axon regeneration, we analyzed axon regeneration 2 days post-SNI when sensory axon regeneration was just starting (Fig. 1h). The results showed that

125 knocking down *UTX* or *JMJD3* in sensory neurons markedly enhanced axon regeneration *in vivo* (Fig.
126 1i-l). Together, these results demonstrated clearly that H3K27 demethylases UTX and JMJD3 were
127 important repressors of sensory axon regeneration.
128
129 ***UTX* knockout enhances optic nerve regeneration and RGC survival**
130 Since the role of UTX in sensory axon regeneration has been confirmed, we further used optic
131 nerve regeneration to explore how UTX regulated CNS neural regeneration. When the levels of UTX
132 and H3K27me3 were examined in the retina after optic nerve crush (ONC), the results showed that the
133 protein level of UTX in RGCs was unchanged (Extended Data Fig. 1a, b), whereas the level of
134 H3K27me3 was transiently decreased 1 day after ONC (Extended Data Fig. 1c, d). To examine the
135 mRNA levels of *UTX* in RGCs, we enriched the Thy1.2 positive RGCs by immunomagnetic cell
136 separation (MACS) and the positive rate of Thy1.2 in positive fraction was 80.8±4.43% based on flow
137 cytometric analysis (Extended Data Fig. 1e, f). Real time PCR analysis showed that the mRNA levels
138 of *UTX* in RGCs were not changed by ONC (Extended Data Fig. 1g), confirming the immunostaining
139 results. By using an available single-cell RNA-seq (scRNA-seq) dataset of adult mouse RGCs[52], we
140 further confirmed that the expression levels of UTX in RGCs were unchanged at different time points
141 after ONC (Extended Data Figure 5a, b). The unchanged levels of UTX in RGCs upon ONC were in
142 stark contrast to that occurred in sensory neurons upon SNI, suggesting that UTX in RGCs might act
143 to suppress optic nerve regeneration.
144 To assess how UTX regulated optic nerve regeneration, we obtained the *UTX* floxed mice.
145 Because *UTX* gene is located in the X chromosome, the female mice have both alleles of *UTX* floxed
146 ($UTX^{f/f}$), whereas the male mice having only allele floxed with *UTY* gene at the other allele ($UTX^{f/y}$).

147 *UTX* were knocked out by intravitreal injection of adeno-associated virus (AAV2) vector encoding the
148 Cre recombinase. The transduction rate of AAV2-Cre in RGCs was 88.8 ± 7.56% (n=2 retinas),
149 evaluated by co-immunostaining the whole mount retina with antibodies against Tuj1 and Cre
150 (Extended Data Fig. 2). The mRNA level of *UTX* in the purified RGCs from the *UTX*$^{f/f}$/AAV2-Cre
151 mice was markedly downregulated compared with that from the control *UTX*$^{f/f}$/AAV2-GFP mice
152 (Extended Data Fig. 3a). In consistent, immunostaining analysis 2 weeks after viral infection showed
153 significantly reduced level of UTX in RGCs in AAV2-Cre injected retinas (Extended Data Fig. 3b, c).
154 As expected, deleting the demethylase UTX resulted in significantly elevated level of H3K27me3 in
155 RGCs (Extended Data Fig. 3d, e). To determine how knocking out *UTX* in RGCs affect RGC survival
156 and optic nerve regeneration, we performed ONC two weeks after the virus injection in either
157 *UTX*$^{f/f}$/AAV2-Cre mice or the control mice (wild type littermate mice injected with AAV2-Cre). Two
158 weeks after ONC, RGC axons were labeled anterogradely by intravitreal injection of the Alexa-594-
159 conjugated cholera toxin β (CTB) and optic nerve regeneration was assessed (Fig. 2a). Fluorescence
160 3D images of tissue-cleared optic nerves were acquired with confocal microscopy as described in our
161 previous study.[53] Wild type mice showed minimal optic nerve regeneration passing the crush sites,
162 whereas knocking out *UTX* in female mice significantly promoted optic nerve regeneration (Fig. 2a-
163 c). Knocking out *UTX* in male mice also induced enhanced optic nerve regeneration, but to a much
164 lesser degree (Fig. 2a-c), likely due to the presence of *UTY* gene in the Y chromosome, which has been
165 shown to have demethylase activity.[54] Furthermore, we obtained UTX enzyme-dead knockin mice
166 (UTX-mut KI) which possess the H1146A and E1148A point mutations in exon 24.[55] To investigate
167 the role of UTX enzymatic activity in optic nerve regeneration, we first performed ONC in either UTX-
168 mut KI mice or the control mice (wild type). Two weeks later, optic nerve regeneration was analyzed

169 by quantifying the number of CTB-594 labeled axons (Fig. 2d). The number and length of regenerating
170 axons in UTX-mut KI mice were enhanced significantly compared to those in wild type mice,
171 suggesting that histone demethylase activity of UTX played a functional role in optic nerve
172 regeneration (Fig. 2d-f). Tissue clearing and 3D imaging allowed us to perform detailed analyses of
173 axonal tip morphology and axon trajectory at the single axon level. As described in our previous
174 study[53], we first quantified the sizes of the distal axon ends of each regenerating axon. We found that
175 UTX deletion significantly reduced the sizes of the distal axon ends, compared to wild type (Fig. 2g,
176 Extended Data Fig. 4). Specifically, in wild type mice, the majority of weakly regenerated short axons
177 had bulbous structures at the distal tips. About 20% of the axons formed the bigger terminal swellings
178 (tip/shaft ratio > 4) defined as retraction bulb-like structures, which are the characteristic structures of
179 non-regenerating axons (Fig. 2g). In contrast, most regenerating axons in male or female mice with
180 UTX deletion showed slim growth cones (Fig. 2g, Extended Data Fig. 4), leading to enhanced axon
181 extension. Furthermore, detailed analysis of axon trajectory showed that in either wild type or *UTX*
182 knockout mice, within the optic nerve regenerating axons often had a meandering path and many of
183 them made U-turns (Fig. 2h, Extended Data Fig. 4), indicating the inhibitory nature of the mature
184 visual system. Interestingly, deleting *UTX* seemed to enhance the U-turn rate, likely due to increased
185 number of regenerating axons. Next, we investigated whether UTX affected the RGC survival with
186 two widely used in vivo cell death models, including the ONC and the NMDA models. When RGC
187 survival was examined 2 weeks post-ONC, the results showed that knocking out *UTX* in either female
188 or male mice significantly protected RGCs from apoptosis (Fig. 2i, j). In the NMDA damage model,
189 deleting *UTX* also markedly increased RGC survival (Fig. 2k, l).

190 To explore the potential of translational application, we tested whether a delayed inhibition of
191 UTX in RGCs after the injury could also promote optic nerve regeneration. We used GSK-J4, a small
192 molecule catalytic site inhibitor selective for the H3K27me3-specific demethylase subfamily (*UTX*
193 and *JMJD3*).[56] GSK-J4 was injected intravitreally every 3 days for 2 weeks after the ONC. The
194 immunostaining result showed that GSK-J4 treatment significantly increased H3K27me3 levels in
195 RGCs, indicating the inhibitory effect on UTX and/or JMJD3 (Fig. 3a, b). When axon regeneration
196 was examined, the results showed that in control mice DMSO had little effect on optic nerve
197 regeneration, whereas significant regeneration was observed in mice with GSK-J4 treatment (Fig. 3c,
198 d). The average lengths of the top 5 longest regenerating axons in mice injected with GSK-J4 were
199 markedly longer than those in control mice with DMSO injection (Fig. 3e). Similar to that of *UTX*
200 knockout, delayed pharmacological inhibition of UTX also promoted RGC survival (Fig. 3f, g).
201 Collectively, these results indicated that deleting demethylase UTX was a novel and effective approach
202 to enhance both optic nerve regeneration and neuronal survival after axonal injury.

203 We next assessed the effects of deleting *JMJD3* in adult RGCs on optic nerve regeneration.
204 The expression pattern of JMJD3 within RGCs was firstly analyzed at different time points after ONC.
205 The dot plot and violin plot obtained from scRNA-seq dataset[52] showed that the mRNA level of *JMJD3*
206 was increased upon ONC (Extended Data Figure 5a, c). By performing immunofluorescence staining,
207 we further confirmed the upregulation of JMJD3 in RGCs after ONC (Extended Data Figure 5d, e).
208 Real time PCR result showed that AAV2-Cre infection of *JMJD3* floxed mice led to significant
209 reduced level of *JMJD3* mRNA level in enriched RGCs compared with that of AAV2-GFP (Extended
210 Data Fig. 6a). To our surprise, the level of H3K27me3 in RGCs was not significantly changed
211 (Extended Data Fig. 6b, c). When optic nerve regeneration was quantified, knocking out *JMJD3* did

212 not significantly increase the number of regenerating axons at different distances from the crush site
213 (Extended Data Fig. 6d, e). However, the average lengths of the top 5 longest regenerating axons in
214 *JMJD3* knockout mice were slightly but significantly longer than that of wild type mice (Extended
215 Data Fig. 6f). Moreover, when both *UTX* and *JMJD3* were knocked out, there was no additive
216 promoting effect on optic nerve regeneration (Extended Data Fig. 6d, g, h). Although deleting *JMJD3*
217 had very minor promoting effect on regeneration, it significantly enhanced RGC survival, and double
218 knocking out *UTX* and *JMJD3* showed additive effect on RGC survival (Extended Data Fig. 6i, j).
219

220 ***UTX* knockout enhanced optic nerve regeneration via distinct pathways from that of PTEN**
221 **deletion**

222 Activation of the mammalian target of rapamycin (mTOR) signaling in adult RGCs is one of
223 the major pathways for promoting optic nerve axon regeneration downstream of several genes, such
224 as PTEN, Lin28, Osteopontin, and Akt/GSK3, etc.[57] Thus, we investigated if UTX deletion also
225 enhanced optic nerve regeneration through the same pathway. Immunostaining of retina sections
226 showed that at 3 days after injury, deleting *UTX* alone in RGCs had no effect on the percentage of
227 phospho-S6 (p-S6) positive RGCs (Fig. 4a, b), whereas UTX/PTEN co-deletion dramatically increased
228 the percentage of p-S6+ RGCs (Fig. 4c, d). In addition, the level of H3K27me3 was significantly
229 elevated in *UTX/PTEN* double knockout RGCs (Fig. 4e, f). These results indicated that *UTX* knockout
230 led to novel downstream signaling pathways distinct from that of PTEN deletion and mTOR activation.
231 We therefore examined the effects of co-deleting *UTX* and *PTEN* in adult RGCs on optic nerve
232 regeneration. AAV2-Cre were injected into the vitreous body of $PTEN^{f/f}$ or $PTEN^{f/f}/UTX^{f/f}$ mice to
233 delete *PTEN* or *PTEN*/*UTX*. Real-time PCR analysis showed that the mRNA levels of both *UTX* and

234 *PTEN* were significantly reduced in *PTEN*/*UTX* double knockout mice (Extended Data Fig. 7a). Optic
235 nerve regeneration was examined 2 weeks after the ONC. The results showed that concomitant deletion
236 of PTEN and UTX in adult RGCs triggered faster optic nerve regeneration and more regenerative
237 axons, compared with PTEN deletion alone (Fig. 4g-i). At 2 weeks after ONC, some long regenerative
238 axons almost reached the region proximal to optic chiasm (Fig. 4g). Based on whole tissue 3D imaging,
239 we also tracked the trajectories of individual RGC axons in distal region of the optic nerve (Extended
240 Data Fig. 7b). Within the distal optic nerve, many regenerating RGC axons induced by PTEN deletion
241 alone showed wandering trajectories with frequent U-turns (Fig. 4j), similar to that of *UTX* knockout
242 alone (see Fig. 2h). However, the U-turn rate was markedly reduced when *UTX* and *PTEN* were both
243 knocked out (Fig. 4j). Moreover, we noticed that some regenerating RGC axons extended multiple
244 branches from the axonal shafts or at the axon ends (Extended Data Fig. 7b). Quantification of axonal
245 branching showed that compared to PTEN deletion alone, the combination of UTX and PTEN deletion
246 led to increased formation of axon branches (Fig. 4k), indicating enhanced axon growth capacity. The
247 additive effects of *UTX/PTEN* double knockout were persistent to 6 weeks after ONC (Extended Data
248 Fig. 8a-c). In *PTEN* single knockout mice almost no regenerating axons could be identified in the optic
249 chiasm, whereas many regenerating axons in *UTX*/*PTEN* double knockout mice reached and entered
250 the optic chiasm with reduced rate of U turn (Extended Data Fig. 8a, d).

251 To better examine how regenerating axons behaved at the optic chiasm, we performed a distal
252 intra-orbital optic nerve crush that shortened the distance axons needed to grow to reach the optic
253 chiasm (Fig. 4l). At 4 weeks after the injury, in *UTX*/*PTEN* double knockout mice many regenerating
254 axons entered the chiasm, whereas in significant contrast almost no axons in *PTEN* knockout mice
255 reached the chiasm (Fig. 4l, m). Moreover, we observed that in the mice with UTX/PTEN co-deletion,

256 more than 60% of regenerating axons stopped growing or turned back at the entry area of the chiasm,
257 indicating optic chiasm as a significant inhibitory barrier (Fig. 4l, n). For regenerating axons entering
258 the chiasm most of them were found in the ipsilateral optic tract (Fig. 4n, Extended Data Fig. 9),
259 indicating axon misguidance. A few regenerating axons crossed the midline into the contralateral optic
260 tract or extend into the opposite uninjured optic nerve (Fig. 4l, n, Extended Data Fig. 9). We also
261 assessed growth patterns of RGC axons entering the chiasm in *UTX*/*PTEN* double knockout mice
262 (Extended Data Fig. 9). The results showed that within the optic chiasm approximately 20% of axons
263 made sharp turns, and axonal branches were observed in different region (Fig. 4o, p, Extended Data
264 Fig. 9). Notably, RGC axons entering the chiasm showed reduced U-turns and axon branching (Fig.
265 4o, p) compared with those within optic nerve (Fig. 4j, k), suggesting spatial differences of the
266 environment between the two regions.
267

268 **UTX deletion in RGCs triggered activation of developmental-like growth programs**

269 To further gain mechanistic insights into promoting effect of UTX on axon regeneration, we
270 performed RNA sequencing (RNA-seq) of the enriched RGCs across different developmental stages
271 (postnatal day 1, 14 and 21) and at 3 days after injury of adult (P42) wild type (AAV2-GFP) or UTX
272 knockout mice (AAV2-Cre). Dissociated RGCs were labeled with Thy1.2 antibody, subjected to
273 fluorescence-activated cell sorting (FACS) for RGC enrichment, and identified by labelling for Tuj1
274 (Extended Data Fig. 10). Two RNA-seq datasets (13 bulk RNA-seq libraries) were generated from
275 FACS-purified RGCs (Extended Data Fig. 11a). It is widely believed that during neuronal maturation
276 the changes in cellular states at the transcriptional level underlie their ability to support regeneration.
277 Young neurons have strong axon growth ability to form the neural circuits. Mature neurons lose the

278 ability to grow and change to support synaptic function.[58] Significant differentially expressed genes
279 (DEGs) were first recognized by comparing the gene expression profiles between P1 and P14 RGCs,
280 but modest DEGs between P14 and P21 RGCs (Extended Data Fig. 11b, c and e). These results
281 indicated that RGCs changed their cellular states from young to mature between P1 and P14. Gene
282 enrichment ontology (GO) analysis showed that downregulated DEGs in P14 RGCs compared to P1
283 RGCs were associated with axonogenesis, developmental cell growth and neuron projection guidance,
284 supporting that axon growth ability reduced during neuronal maturation (Extended Data Fig. 11d, f).
285 We further compared the transcriptomic profiles of injured adult control or *UTX* knockout RGCs (P42)
286 to RGC maturational datasets. Hierarchical clustering analysis (HCA) revealed that the profiles were
287 grouped into two main clusters with similar gene expression pattern (Fig. 5a). The first cluster included
288 P1, P14 and AAV2-Cre (*UTX* knockout RGCs), while the second cluster involved P21 and AAV2-
289 GFP (control RGCs). In addition, the transcriptomic profiles of injured *UTX* knockout RGCs (AAV2-
290 Cre) was more similar to the P1 and P14 than to wild type control RGCs (AAV2-GFP) and P21 RGCs.
291 Furthermore, principal component analysis (PCA), the linear dimensionality reduction method, was
292 adopted for precisely screening the significantly components and finding potential clusters across all
293 samples. The results showed that the first principal component (Dim 1) contribute the most (60.6%)
294 for explaining the variance (Fig. 5b). *UTX* knockout (AAV2-Cre) clustered close to P1 and had similar
295 features with P14 and P21 along Dim 1 compared to wild type (AAV2-GFP), suggesting the strong
296 commonalities of *UTX* knockout and developmental stage RGCs (Fig. 5b). Next, we identified genes
297 with significant contribution in the PCA clustering, especially relevant to Dim 1. GO enrichment
298 analysis was conducted to reveal the biological roles of genes involved in Dim 1 and 2. As shown in

299 Fig. 5c, Dim 1 explained most variance in the transcriptomic pattern of genes involved in postsynaptic
300 organization, dendrite development, neuron projection organization, and neuron apoptotic process etc.
301 By calculating the z-score of genes contributed to the top 20 enriched GO terms, it showed
302 distinct heterogeneity between wild type and other groups, but significant homogeneity between UTX
303 deletion and P14 (Fig. 5d). Meanwhile, Double hierarchical clustered heatmap showed that many of
304 these genes with top contribution in Dim 1 were associated with activation of developmental and
305 growth programs. For instance, several genes, including EHMT2[59], BRSK1[60], EEF1A2[61] and LRFN4[62],
306 have previously been shown to induce axon initiation, formation, sprouting and outgrowth (Fig. 5e).
307 Thus, this finding suggests that knocking out *UTX* in adult injured RGC triggers reactivation of
308 developmental-like growth programs, leading to an immature cellular state.
309 To further identify gene regulatory networks that control the changes mediated by UTX
310 deletion, we performed a comparative analysis that profiled transcription in enriched RGCs. In total,
311 574 common DEGs were identified (425 significantly upregulated and 149 downregulated) at the
312 thresholds of $|\log_2 FC| > 1$ (FC, fold change) and adjusted P-value of < 0.05 (Fig. 6a, b). Furthermore,
313 GO enrichment analysis indicated that the majority of genes downregulated by UTX deletion were
314 associated with sensory perception, sensory system development, retina homeostasis and response to
315 light stimulus (Fig. 6c), most of which related to mature neuronal functions. On the other hand, the
316 highly enriched GO terms of up-regulated DEGs were mainly related to regulation of virus, response
317 to cytokine and lymphocyte activation (Fig. 6c) that were mostly non-neuronal genes. Several
318 significantly altered genes were involved in axon regeneration (Fig. 6d). For example, KLF4[63], Myc[9]
319 and THBS1[64] has been shown to play crucial roles in controlling on regeneration. Additionally,
320 CaMK2 reactivation can protect RGCs in multiple injury/disease models.[65] Taken together, these

321 results suggested that UTX deletion promoted optic nerve axon regeneration via activating
322 developmental-like growth programs and repressing mature neuron enriched genes.
323
324 **miR-124-5p acts downstream of UTX to regulate optic nerve regeneration**
325 Among repressed genes induced by *UTX* knockout, we focused on *microRNA-124* (*miR-124*),
326 which was one of the most significantly downregulated genes ($\log_2$ FC = -1.897, $P = 2.29\times10^{-13}$,
327 adjusted P-value = 1.18×10^{-10}) in *UTX* knockout mice after injury based on RNA-seq result (Fig. 7a).
328 After *UTX* knockout, all 3 loci encoding miR-124 at different chromosomes had markedly reduced
329 transcription, coincident with closed chromatin structure. *miR-124*, as a highly enriched miRNA in
330 mature neurons, has been shown to play essential roles in neurogenesis and neuronal differentiation
331 during development and cellular reprogramming to neurons.[66-68] There are 2 mature forms of miR-
332 124, miR-124-3p and miR-124-5p. Real time PCR analysis showed that mature miR-124-3p and miR-
333 124-5p levels were both significantly reduced in the enriched RGCs from the retinas of *UTX*$^{f/f}$-AAV2-
334 Cre mice compared to that from the *UTX*$^{f/f}$-AAV2-GFP mice (Fig. 7b, Extended Data Fig. 12a). Thus,
335 we asked whether *miR-124-5p/3p* could be downstream targets of *UTX* to regulate axon regeneration.
336 By using three different search engines (miRDB, TargetScan and miRWalk), we first explored a set of
337 overlapped candidate targets of miR-124-5p or miR-124-3p. The GO analysis of potential miR-124-
338 5p targets showed that enriched terms were involved in synapse organization, developmental growth,
339 axon guidance, axonogenesis and neuron projection extension (Fig. 7c, d), suggesting that miR-124-
340 5p might function to regulate axon regeneration. Therefore, we intravitreally administered *miR-124-*
341 *5p/3p* antagomirs into wild type mice to assess the effects of miR-124 suppression on axon
342 regeneration and neuronal survival. Wild type mice injected with scrambled antagomir was used as

343 the control. Two weeks after ONC, we observed that miR-124-5p suppression led to significant optic
344 nerve regeneration with many regenerating axons extending 1.5 mm from the crush site (Fig. 7e, f).
345 The average lengths of the top 5 longest regenerating axons in the mice with miR-124-5p suppression
346 were significantly longer than those in control mice (Fig. 7g). However, miR-124-5p suppression did
347 not seem to significantly enhance RGC survival (Fig. 7h, i). In contrast to *miR-124-5p*, analysis of
348 potential *miR-124-3p* targets did not show obvious connections to neural development (Extended Data
349 Fig. 12b, c). Indeed, suppressing *miR-124-3p* with specific antagomir did not promote optic nerve
350 regeneration compared with the control group treated with scrambled antagomir (Extended Data Fig.
351 12d, e). Similarly, miR-124-3p suppression showed no effect on RGC survival rate (Extended Data
352 Fig. 12f). Together, these data demonstrated clearly that specific inhibition of *miR-124-5p* but not *miR-*
353 *124-3p* was able to markedly enhance optic nerve regeneration.

354 To confirm that genes encoding *miR-124* were indeed targeted by *UTX* knockout-induced
355 H3K27me3, we performed ChIP-PCR analysis using anti-H3K27me3 on DNA nucleotides upstream
356 of miR-124 gene in the chromosome 3 (see Fig. 7a, miR-124-2). The results revealed that comparing
357 with wild type RGCs, trimethylated histone H3K27me3 showed increased interaction with 3 DNA
358 regions preceding miR-124 (R1-3), especially at R3 region (Fig. 7j).

359 **DISCUSSION**

360 Recent progresses in axon regeneration research have shown that significant changes in gene
361 transcription underlie the regenerative capacity of mammalian PNS neurons, and silence of such
362 genetic programs is responsible for the diminished intrinsic axon regeneration ability of mammalian
363 CNS neurons. Our study provided clear and strong evidence that X chromosome encoded histone
364 deacetylase UTX and its paralog JMJD3, acting as regeneration repressors to regulate spontaneous
365 sensory axon regeneration *in vivo*. More importantly, conditional UTX deletion in RGCs resulted in
366 robust optic nerve regeneration and increased RGC survival via reshaping RGC chromatin and
367 transcriptomic landscape back to a developmental-like state. Interestingly, our results showed that
368 knocking out *UTX*, but not *JMJD3*, significantly promoted optic nerve regeneration after ONC.
369 However, deletion of either UTX or JMJD3 markedly protected RGCs from apoptosis, and deleting
370 both of them showed additive effect on RGC protection. Despite up to 84% of sequence similarity in
371 the JmjC domain between UTX and JMJD3[69], accumulating evidence indicated that they played
372 surprisingly contrasting roles in cellular reprogramming[38, 39], neural commitment[70], skeletal
373 formation[71], embryonic development[72, 73], muscle regeneration[74], lifespan extension[75], plasma cell
374 formation[76] and tumorigenesis[77, 78]. These findings also suggested that the distinct functional roles of
375 UTX and JMJD3 were associated with demethylase-dependent and -independent manners, relative
376 expression, post-translational modifications and complex formation. Thus, further investigations may
377 shed light on their unique physiological roles in axon regeneration and RGC survival.

378 Although many genes have been identified to induce optic nerve regeneration, we have limited
379 knowledge about how neuronal transcriptomics landscape is reshaped during regeneration via
380 epigenetic modification. By performing and analyzing RNA-seq of enriched RGCs at different

381 developmental/maturation stages and between wild type and *UTX* knockout mice, we found that
382 deleting *UTX* in mature RGCs changed their transcriptomic landscape back to a developmental-like
383 state. As a result, mature RGCs regained their intrinsic ability to support axon regeneration. In our
384 latest study[49], we found that H3K27 methyltransferase EZH2 in post-mitotic neurons functioned to
385 repress dendrite development during development. Together with this study, it seems that H3K27me3
386 functions as a major epigenetic regulator of neuronal morphogenesis, promoting axon growth but
387 suppressing dendrite development.

388 Downstream of *UTX* knockout, we identified *miR-124* as targeted genes to regulate optic nerve
389 regeneration. As one of the most abundant microRNAs in mature neurons, miR-124 has been shown
390 to be a key regulator that coordinates multiple genes to control neuronal fate determination during
391 neural development.[66, 68, 79] Moreover, overexpression of miR-124 has been shown to reprogram
392 somatic cells into neurons.[80, 81] It should be noted that these aforementioned functions are regulated by
393 the well-studied miR-124-3p. In contrast, here we showed that mature miR-124-5p, but not miR-124-
394 3p, acted to regulate optic nerve regeneration, revealing a novel function of miR-124. Importantly,
395 epigenetic regulation, such as histone modifications and microRNAs, can orchestrate a large-scale
396 change in gene expression to regulate biological functions. The UTX-miR-124 networks revealed in
397 this study are well positioned to reshape the gene expression landscape of mature CNS neurons at both
398 the transcriptional and translational levels to enhance axon regeneration.

399 Lastly, UTX has been shown to escape from X inactivation and be expressed in the inactivated
400 X chromosome. As a result, the protein level of UTX is higher in female than that in male mice in
401 most cells, including neurons. A recent study[82] showed that UTX contributed to the resistance of
402 neurodegenerative insults of neurons in female mice. Interestingly, based on previous epidemiology

403 studies, it is known that women are more likely to be affected by glaucomatous disease, especially for
404 angle-closure glaucoma (ACG), for which nearly 70% are women.[83, 84] Our study raised the possibility
405 that higher level of UTX in female RGCs might increase the susceptibility of female animal to retinal
406 injury.

407 **EXPERIMENTAL PROCEDURES**

408 **Animals**

409 All experiments involving animals were performed in accordance with the animal protocol
410 approved by the Institutional Animal Care and Use Committee of the Johns Hopkins University,
411 Chinese Academy of Sciences and Zhejiang University. 8- to 12-week old adult female CF-1 mice
412 (weighing from 30 to 35 g) were purchased from Charles River Laboratories and housed in the
413 University Animal Facility. The female *UTX*$^{f/f}$ mutant mice (Kdm6atm1c(EUCOMM)Jae) possessing
414 loxP sites flanking exon 3 of the Kdm6a (lysine (K)-specific demethylase 6A) gene, the *JMJD3*$^{f/f}$
415 mutant mice (B6.Cg-Kdm6btm1.1Rbo/J) possessing loxP sites flanking exons 14-20 of the Kdm6b
416 (lysine (K)-specific demethylase 6B) gene and the *PTEN*$^{f/f}$ mutant mice (B6.129S4-Ptentm1Hwu/J)
417 possessing loxP sites flanking exon 5 of the Pten (phosphatase and tensin homolog) gene were
418 purchased from The Jackson Laboratory. *UTX* enzyme-dead knockin mice possessing the H1146A and
419 E1148A point mutations in exon 24, as a gift, were obtained from Dr. Kai Ge at the National Institutes
420 of Health.

421

422 **Immunostaining, fluorescence microscopy, and image analysis**

423 The DRG or retina cryostat sections were collected and immunostained with the antibody
424 against H3K27me3 (1:1000), UTX (1:500), JMJD3 (1:500), or p-S6 (1:500) each co-immunostained
425 with the neuronal marker Tuj1 (1:1000) antibody. To quantify the fluorescence intensity of H3K27me3,
426 UTX, JMJD3, or p-S6 in sensory neurons, only Tuj1 positive cells were selected for measurement.
427 The mean fluorescence intensity of each sensory neuron in DRG or RGC in retina section was
428 measured using the ImageJ software. The percentage of p-S6 positive RGCs was calculated by dividing

429 the number of p-S6/Tuj1 double positive cells by the number of Tuj1 positive cells. For DRG, 3
430 independent DRG tissues in each condition were used in each condition. For each DRG, 3 sections
431 were selected and 30 sensory neurons in each section were selected for measurement. For retina, 3
432 independent retinal tissues in each condition were used. For each retina, 3-8 sections were selected and
433 15-20 RGCs in each section were selected for measurement. The "n" in the figures indicates the
434 number of independent experiments.
435

436 **In vivo electroporation of adult DRG neurons and quantification of axon regeneration**

437 The in vivo electroporation of adult mouse DRGs was performed as described previously.[51]
438 Briefly, under anesthesia induced by katamine (100 mg/kg) and xylazine (10 mg/kg), a small
439 dorsolateral laminectomy was performed to expose the L4 and L5 DRGs. EGFP plasmid or EGFP plus
440 siRNA oligos (1-1.5 μl per ganglion) were injected into the DRGs using pulled glass capillaries and a
441 Picospritzer II (Parker Ins.; pressure, 30 psi; duration: 8 ms). Immediately after injection,
442 electroporation was performed by applying five pulses of current (35 V, 10 msec, 950-msec interval)
443 using a custom-made tweezer-like electrode powered by the Electro Square Porator ECM830 (BTX
444 Genetronics). The mice were allowed to recover after closing the wound. Two days after the
445 electroporation, the sciatic nerves were crushed with fine forceps and the crushed sites were marked
446 with nylon epineural sutures (size 10-0). Two days later, the mice were perfused with ice-cold 4% PFA
447 in sodium phosphate buffer (pH 7.4). The whole nerve segment was then dissected out and further
448 fixed in 4% PFA overnight at 4°C. Before whole-mount flattening, it was confirmed that the place of
449 epineural suture matched the injury site, and experiments were included in the analysis only when the
450 crush site was clearly identifiable.

451 For quantification of in vivo axon regeneration, the fluorescence images of the whole mount
452 nerves were first obtained. All identifiable EGFP-labeled axons in the sciatic nerve were then manually
453 traced from the crush site to the distal growth cone to measure the length of axon regeneration. Only
454 nerves with at least 15 identifiable axons were measured, and the "n" in the figures indicates the
455 number of mice.
456

457 **Quantitative real time polymerase chain reaction (Real time-PCR)**

458 Total RNA was isolated with the TRizol Reagent (Thermo Fisher Scientific), then reverse
459 transcribed by using the M-MLV reverse transcriptase (Roche Applied Science). To quantify the
460 mRNA levels with real time PCR, aliquots of single-stranded cDNA were amplified with gene-specific
461 primers and Power SYBR Green PCR Master Mix (Invitrogen) using the CFX96™ real time PCR
462 detection system (Bio-Rad). Specific primers used in this study are listed in Extended Data table 1.
463 The PCR reactions contained 20-40 ng of cDNA, Universal Master Mix (Invitrogen), and 200 nM of
464 forward and reverse primers in a final reaction volume of 20 µl. The ratio of different samples was
465 calculated by the build in data analysis software of the CFX96™ real time PCR system.
466

467 **Intravitreal injection, optic nerve crush, and RGC axon anterograde labeling**

468 The mice were anaesthetized with intra-peritoneal injection of a mixture of ketamine (100
469 mg/kg) and xylazine (10 mg/kg). 1 µl of AAV2 viruses (Titers > $1x10^{13}$ vg/ml), GSK-J4 (300 mM),
470 or antagomirs (556 mM), 1.5 µl NMDA (20 mM) for NMDA-induced retinal neurotoxicity were
471 injected into the vitreous body of 6- to 8-week old mutant or wild type mice by glass micropipette
472 connected to a Picospritzer II (Parker Inc.) (pressure: 15 psi; duration: 6 ms). Two weeks after

473 intravitreal injection, the right optic nerve was exposed intraorbitally and crushed with Dumont #5
474 forceps for 5 seconds approximately 1 mm behind the optic disc.

475 To label RGC axons in the optic nerve by anterograde labeling, 1.5 μl of cholera toxin β subunit
476 (CTB) conjugated with fluorescence Alexa-594 (2 μg/μl, Invitrogen) was injected into the vitreous 2
477 days before sacrificing the animals. Sacrificed animals were fixed by perfusion with 20 mL of 0.1 M
478 phosphate buffered saline (PBS), followed with 40 mL of 4% paraformaldehyde (PFA) at 5 ml/minute.
479 Retina and optic nerve segments were dissected out and post-fixed in 4% PFA overnight at 4 °C. The
480 fixed optic nerves were rinsed with cold PBS three times and stored in cold PBS until further use.

481

482 **Tissue dehydration and clearing**

483 Optic nerves were first dehydrated in increasing concentrations of tetrahydrofuran (THF, 50%,
484 70%, 80%, 100% and 100% for 20 minutes each) in amber glass bottles as described in a previous
485 publication.[85] Incubations were carried out on an orbital shaker at room temperature. Optic nerves were
486 then transferred into benzyl alcohol/benzyl benzoate (BABB, 1:2 in volume; Sigma) clearing solution
487 for 20 minutes. During the whole procedure optic nerves were protected from light to reduce the loss
488 of CTB fluorescent signal.

489

490 **Imaging and quantification of RGC axon regeneration in the optic nerve**

491 The whole-mount cleared optic nerves were imaged using a Zeiss LSM 710 confocal
492 microscope controlled by ZEN software. A 20X objective was used to acquire image stacks with 2-
493 μm z spacing. The Motor-driven XY scanning stage with tiling function were used to scan the optic
494 nerve with 15% overlap in the X Y dimensions. The 3D image was created by Imaris 9.2 (Bitplane).

495 For quantification of optic nerve axon regeneration, every 4 consecutive images were projected
496 to generate a series of Z-projection images of 8-μm optical sections. In each Z-projected image, the
497 number of CTB-labeled fibers was counted at 250-μm intervals distal to the crush site till the place
498 where no fluorescence signals were visible. The numbers at each 250-μm intervals were summed over
499 all Z-projection images.

500 For quantification of the average lengths of top 5 longest regenerating axons, all acquired
501 images were merged together using ZEN software to generate the maximum intensity Z-projection
502 images. Then the lengths of the top 5 longest axons were manually measured from the ends to the
503 crush site with ImageJ software (NIH).

504

505 **Analyses of axonal tip morphology and axon trajectory**

506 The analysis of axonal tip morphology was performed as described previously.[86] For
507 quantification of the size of the distal axon ends, the tips of top 20 longest regenerating axons were
508 identified in the Z-projection images of each nerve. Using ImageJ software (NIH), the maximal width
509 of the axonal tips was measured and was presented as a ratio with respect to the diameter of the adjacent
510 axon shaft (tip/axon shaft ratio). The axon ends with tip/axon shaft ratio > 4 were defined as retraction
511 bulb, while the others as growth cone.

512 For quantification of the U-turn rate, in the Z-projection images the trajectories of top 20
513 longest axons within optic nerve or all axons entering the optic chiasm were tracked near the axonal
514 ends. The axonal trajectory that made a turning with the angle between the direction of the axonal tip
515 and the longitudinal axis of the optic nerve greater than 90 degrees was defined as a U-turn. The U-
516 turn rate of each nerve was presented by U-turn number/axon number.

517 For quantification of branching index, in the Z-projection images the axonal tips number was
518 counted from the selected site (with 20 regenerating axons passing or the optic nerve-chiasm transition
519 zone) till the place where no tips were visible. The branching index of each nerve was calculated by
520 axonal tips number/selected axon number (20 axons for optic nerve or all axons for the optic chiasm).
521

522 **Quantification of RGC transduction and survival rates**

523 Retinas were dissected out for whole-mount preparations. Retinal whole-mounts were blocked
524 in the staining buffer containing 2% BSA and 0.5% Triton X-100 in PBS for 1 hour before incubation
525 with primary antibodies. Primary antibodies used: Tuj1 (1:500), Cre (1:500). Retinas were incubated
526 with primary antibodies overnight at 4°C and washed four times for 10 minutes each in PBS containing
527 0.5% Triton X-100. For secondary antibodies, Alexa Fluor-488/647-conjugated antibodies were used.
528 Confocal images were acquired using a Zeiss LSM 710 confocal microscope (20X objective). Images
529 were organized and analyzed using ZEN and ImageJ software. For RGC survival quantification,
530 whole-mount retinal tissues were immunostained with Tuj1 antibody to label the survival RGCs. 15-
531 20 fields were randomly sampled from the peripheral regions of each retina. The survival rate was
532 calculated by measuring the ratio of Tuj1 positive cell number in retina with optic nerve crush (ONC)
533 to that in control retina without ONC. To quantify RGC transduction efficiency by AAV2-Cre, whole-
534 mount retinal tissues were double-immunostained with Tuj1 and Cre antibodies. 8-12 fields were
535 randomly sampled from the peripheral regions of each retina. The transduction efficiency was
536 calculated by counting and calculating the ratio of Cre/Tuj1 double-positive cell number to the number
537 of Tuj1 positive cells.
538

539 **Western blot**

540 Total protein was extracted with the RIPA buffer containing protease inhibitor cocktail and
541 phosphatase inhibitor cocktail. 15 μg of each protein sample was separated by a 4-12% gradient SDS-
542 PAGE gel and electrotransferred onto polyvinylidene fluoride membranes. Nonspecific bands were
543 blocked with 5% non-fat milk in 1x TBS containing 0.1% tween-20 (TBST) for 1 hour at room
544 temperature. Membranes were incubated with the primary antibodies of H3K27me3 (1:1000), H3
545 (1:5000), UTX (1:1000), JMJD3 (1:1000), β-actin (1:10000) as internal control overnight at 4 °C and
546 followed by HRP-conjugated secondary antibodies with a concentration of 1:2000 for 1 hour at room
547 temperature. Membranes were washed with TBST for 15 minutes three times after each antibody
548 incubation. The immunocomplex bands were visualized by the ECL kit (GE Healthcare), then analyzed
549 with the ImageJ software (NIH). The relative protein level of each target was calculated by first
550 normalizing to the internal control, and then the control group.

551

552 **Purification of RGCs**

553 Retinas were dissected, incubated with 20 units/ml papain and 0.005% DNase (Worthington)
554 for 10 minutes at 37 °C, then dissociated into a single-cell suspension in pre-sort buffer (BD FACS).
555 Retinal cells were filtered through a 40-μm cell strainer (BD Falcon), then collected by centrifugation
556 at 500 g for 5 minutes. Supernatant was removed and immediately pelleted cells were resuspended in
557 400 μl of pre-sort buffer. Cell suspension was incubated with Fc block antibodies for 5 minutes at 4°C
558 and then stained with Thy1.2-FITC antibody and IgG2a isotype antibody (Thermo fisher) as a negative
559 control for 30 minutes at 4 °C, respectively. Retinal cells were pelleted by centrifugation at 500 g for
560 5 minutes. Supernatant was discarded and pelleted cells were washed one time with 500 μl of pre-sort

561 buffer. Cell suspension was incubated with DAPI for 5 minutes before FACS sorting, and then sorted
562 on a BD FACSAria Fusion using a 100-micron nozzle. Sorted cells were immediately subjected to
563 subsequent experiments.

564 For RGC enrichment by immunomagnetic cell separation (MACS), cell suspension was
565 incubated with Fc block antibodies for 5 minutes at 4 °C and then labeled with anti-mouse Thy1.2
566 magnetic particles (BD IMag™) for 30 minutes at 4 °C. Tubes were placed on the cell separation
567 magnet at room temperature for 8 minutes (BD IMag™), then the supernatant was aspirated off
568 carefully for leaving unlabeled cells. Labeled cells were resuspended in 1x BD IMag™ buffer and the
569 tubes were returned to the magnet for another 4 minutes. The separation was repeated twice to increase
570 the purity of the positive fraction. After the final wash step, purified cells were immediately used for
571 further analyses.

572

573 **Library preparation and RNA sequencing**

574 A total amount of 2 μg RNA per sample was used as input material for the RNA sample
575 preparations. Sequencing libraries were generated using NEBNext® Ultra™ RNA Library Prep Kit
576 for Illumina® (#E7530L, NEB, USA) following the manufacturer's recommendations and index codes
577 were added to attribute sequences to each sample. Briefly, mRNA was purified from total RNA using
578 poly-T oligo-attached magnetic beads. Fragmentation was carried out using divalent cations under
579 elevated temperature in NEBNext First Strand Synthesis Reaction Buffer (5X). First strand cDNA was
580 synthesized using random hexamer primer and RNase H. Second strand cDNA synthesis was
581 subsequently performed using buffer, dNTPs, DNA polymerase I and RNase H. The library fragments
582 were purified with QiaQuick PCR kits and elution with EB buffer, then terminal repair, A-tailing and

583 adapter added were implemented. The aimed products were retrieved and PCR was performed, then
584 the library was completed.

585 RNA concentration of library was measured using Qubit® RNA Assay Kit in Qubit® 3.0 to
586 preliminary quantify and then dilute to 1 ng/μl. Insert size was assessed using the Agilent Bioanalyzer
587 2100 system (Agilent Technologies, CA, USA), and qualified insert size was accurate quantification
588 using StepOne Plus™ real-time PCR System (Library valid concentration > 10 nM). The clustering of
589 the index-coded samples was performed on a cBot cluster generation system using HiSeq PE Cluster
590 Kit v4-cBot-HS (Illumina) according to the manufacturer's instructions. After cluster generation, the
591 libraries were sequenced on an Illumina platform and 150 bp paired-end reads were generated.
592

593 **Bulk RNA-seq data analysis**

594 Using bulk RNA-seq, we measured gene expression profiles of UTX-AAV-Cre, UTX-AAV-
595 GFP, and postnatal day (P) 1, P14, P21 samples, with at least two biological replicates for each
596 condition or timepoint. All raw sequencing reads were quality checked with FastQC (v0.11.9), and
597 leading bases were trimmed from the reads with Trimmomatic (v0.39) as appropriate. Quality-checked
598 reads were mapped to the GRCm38/mm10 mouse reference genome with splice-aware aligner
599 HISAT2 (v2.2.1). featureCounts (Subread v2.0.3) was used to estimate the expression counts of the
600 genes.

601 For differential gene expression analysis, we used DESeq2 (v1.34.0) to perform normalization
602 and differential expression test on the raw read counts for each gene. Differential expression genes
603 (DEGs) were defined using DESeq2 with the adjusted P-value < 0.05 and $|\log_2(\text{Fold Change})| > 1$. The
604 gene ontology (GO) enrichment analysis was performed by clusterProfiler (v4.2.2). In order to
605 integrate and analyze UTX knockout data and optic nerve development data, The TPM (transcriptsper

606 million reads) matrix for genes and transcripts calculated by RSEM (v1.3.3) were used. We also used
607 the ComBat in sva (v3.42.0) to minimize the technical effect of different data. The corrected values
608 were subjected to principal components analysis (PCA) and hierarchical clustering.
609
610 **Single-cell RNA-seq data analysis**
611 The data used to analyze the time course of transcriptomic changes in single retinal ganglion
612 cells following optic nerve crush was downloaded from Gene Expression Omnibus (GEO:
613 GSE137398). Then, the expression matrices were integrated by Seurat (v4.1.0) with default parameters.
614 The changes of average expression levels of *UTX (Kdm6a)* and *JMJD3 (Kdm6b)* in all RGCs were
615 mainly analyzed at different time point after ONC, as showed in dot plot and violin plot.
616
617 **Cut&Tag**
618 Approximately $1x10^5$ RGCs purified by coupling Thy 1.2 beads were processed by
619 centrifugation, and were washed with Wash Buffer (20 mM HEPES, pH 7.5; 150 mM NaCl; 0.5 mM
620 Spermidine; 1X Protease inhibitor cocktail; 0.05% DMSO-Digitonin). The supernatant was removed
621 and the bead-bound cells were resuspended with 50 μL Dig-wash Buffer (20 mM HEPES, pH 7.5; 150
622 mM NaCl; 0.5 mM Spermidine; 1x Protease inhibitor cocktail; 0.05% DMSO-Digitonin) containing 2
623 mM EDTA and 1% BSA and a 1 : 50 dilution of the primary antibody. Primary antibody incubation
624 was performed on a rotating platform for 2h at room temperature. The primary antibody was removed
625 by transient centrifugation and placing the tube on the magnet stand to clear and pulling off all the
626 liquid. The appropriate second antibody was diluted 1 : 50 in 50 μL Dig Wash Buffer and bead-bound
627 cell were incubated for 1h at room temperature. Cells were washed using the magnet stand 2 times for

628 5min in 200 μL Dig-Wash buffer to remove unbound antibodies. A 1 : 200 dilution of pG-Tn5 adapter
629 complex (~0.04 μM) was prepared in Dig-300 Buffer (0.05% DMSO-Digitonin, 20 mM HEPES, pH
630 7.5, 300 mM NaCl, 0.5 mM Spermidine, 1x Protease inhibitor cocktail). After removing the liquid on
631 the magnet stand, 100 μL was added to the cells with gentle vortexing, which was incubated with pG-
632 Tn5 at RT for 1 h. Cells were washed 2 times for 5min in 200 μL Dig-300 Buffer to remove unbound
633 pG-Tn5 protein. Next, cells were resuspended in 300 μL Tagmentation Buffer (10 mM MgCl 2 in Dig-
634 300 Buffer) and incubated at 37 °C for 1h. To stop tagmentation, 2.25 μL of 0.5 M EDTA, 2.75 μL of
635 10% SDS and 0.5 μL of 20 mg/mL Proteinase K was added to 300 μL of sample, which was incubated
636 overnight at 37 °C. To extract the DNA, 300 μL PCI (Phenol : Chloroform : Isoamylol = 25 : 24 : 1)
637 were added to each sample with vortexing, quickly spun 5s ,16000g for 15 min at room temperature.
638 Absorbed the upper water phase to a new 1.5 mL tube and added 300 chloroform, 16000 g for 15 min
639 at room temperature. Absorbed the upper water phase to a new 1.5 mL tube and added 700 μL 100%
640 ethyl alcohol, 16000g for 15 min at 4 °C. Pulled off all the liquid and added 1 mL 100% ethyl alcohol
641 16000g for 1 min at 4 °C. Carefully discarded all the liquid and aired the tube 5 min, 25 μL 1X TE
642 （10 mM Tris-HCl, pH 8.0) containing 1 mM EDTA were added to dissolve the DNA. To amplify
643 libraries, 24 μL DNA was mixed with 5 μL a uniquely index i7 and i5 primer; Using a different index
644 for each sample. A volume of 16 μL PCR Master mix was added and mixed. The sample was placed
645 in a Thermocycler with a heated lid using the following cycling conditions: 72 °C for 3 min ; 98 °C
646 for 30 s; 17 cycles of 98 °C for 10 s and 60 °C for 30s and 72 °C for 30s; final extension at 72 °C for
647 5 min and hold at 4 °C. Post-PCR clean-up was performed by adding 1.1× volume of DNA clean beads
648 (Nanjing, vazyme), and libraries were incubated with beads for 15 min at RT, washed twice gently in
649 80% ethanol, and eluted in 20 μL sterile water.

650 **Statistics**

651 Statistics were analyzed using GraphPad Prism 7.0 and the significance was set at a value of p
652 < 0.05. Data are presented as mean ± SEM. For two group comparisons, if the data were normalized
653 to the control condition and presented as percentage of control, one sample t test was used to determine
654 the statistical significance. Otherwise, the regular two tailed student's t test was used. For comparison
655 between multiple groups, the one-way ANOVA followed by Tukey's multiple comparison test was
656 used to determine the statistical significance. The "n" indicates the number of independent experiments
657 unless specifically stated otherwise.

658 **Author Contributions**

659 S-G. Y., C-M. L., and F-Q. Z. initiated the projects and designed the experiments. S-G. Y., X-
660 W. W., and C-P. L. performed most of experiments and analyzed data. T. H. performed most of the
661 bioinformatics analyses. Q. L. and L-R. Z., C. Q., S. performed experiments and analyzed the data. J.
662 Q. helped with the bioinformatic analyses. S-G.Y. and F-Q.Z. wrote the manuscript with inputs from
663 all the authors.

664

665 **Acknowledgements**

666 The study was supported by grants (to F.Q.Z.) from NIH (R01NS085176), the Craig H. Neilsen
667 Foundation (259450), and the BrightFocus Foundation (G2017037), as well as the grants (to C.-M.L.)
668 from Maryland Stem Cell Research Fund and the National Science Foundation of China (No.
669 81571212).

670 **Reference**

671 1 He Z, Jin Y. Intrinsic Control of Axon Regeneration. *Neuron* 2016; **90**:437-451.
672 2 Qian C, Zhou FQ. Updates and challenges of axon regeneration in the mammalian central nervous system. *J*
673 *Mol Cell Biol* 2020; **12**:798-806.
674 3 Yang SG, Li CP, Peng XQ, Teng ZQ, Liu CM, Zhou FQ. Strategies to Promote Long-Distance Optic Nerve
675 Regeneration. *Front Cell Neurosci* 2020; **14**:119.
676 4 Moore DL, Blackmore MG, Hu Y *et al.* KLF family members regulate intrinsic axon regeneration ability. *Science*
677 2009; **326**:298-301.
678 5 Blandini F, Bazzini E, Marino F *et al.* Calcium homeostasis is dysregulated in parkinsonian patients with L-
679 DOPA-induced dyskinesias. *Clin Neuropharmacol* 2009; **32**:133-139.
680 6 Smith PD, Sun F, Park KK *et al.* SOCS3 deletion promotes optic nerve regeneration in vivo. *Neuron* 2009;
681 **64**:617-623.
682 7 Sun F, Park KK, Belin S *et al.* Sustained axon regeneration induced by co-deletion of PTEN and SOCS3. *Nature*
683 2011; **480**:372-375.
684 8 O'Donovan KJ, Ma K, Guo H *et al.* B-RAF kinase drives developmental axon growth and promotes axon
685 regeneration in the injured mature CNS. *J Exp Med* 2014; **211**:801-814.
686 9 Belin S, Nawabi H, Wang C *et al.* Injury-induced decline of intrinsic regenerative ability revealed by
687 quantitative proteomics. *Neuron* 2015; **86**:1000-1014.
688 10 Nathan FM, Ohtake Y, Wang S *et al.* Upregulating Lin28a Promotes Axon Regeneration in Adult Mice with
689 Optic Nerve and Spinal Cord Injury. *Mol Ther* 2020; **28**:1902-1917.
690 11 Wang XW, Li Q, Liu CM *et al.* Lin28 Signaling Supports Mammalian PNS and CNS Axon Regeneration. *Cell*
691 *Rep* 2018; **24**:2540-2552 e2546.
692 12 Zhang Y, Williams PR, Jacobi A *et al.* Elevating Growth Factor Responsiveness and Axon Regeneration by
693 Modulating Presynaptic Inputs. *Neuron* 2019; **103**:39-51 e35.
694 13 Minarovits J, Banati F, Szenthe K, Niller HH. Epigenetic Regulation. *Adv Exp Med Biol* 2016; **879**:1-25.
695 14 Strickland IT, Richards L, Holmes FE, Wynick D, Uney JB, Wong LF. Axotomy-induced miR-21 promotes axon
696 growth in adult dorsal root ganglion neurons. *PLoS One* 2011; **6**:e23423.
697 15 Jiang JJ, Liu CM, Zhang BY *et al.* MicroRNA-26a supports mammalian axon regeneration in vivo by
698 suppressing GSK3beta expression. *Cell Death Dis* 2015; **6**:e1865.
699 16 Liu CM, Wang RY, Saijilafu, Jiao ZX, Zhang BY, Zhou FQ. MicroRNA-138 and SIRT1 form a mutual negative
700 feedback loop to regulate mammalian axon regeneration. *Genes Dev* 2013; **27**:1473-1483.
701 17 Li S, Zhang R, Yuan Y *et al.* MiR-340 Regulates Fibrinolysis and Axon Regrowth Following Sciatic Nerve Injury.
702 *Mol Neurobiol* 2017; **54**:4379-4389.
703 18 Motti D, Lerch JK, Danzi MC *et al.* Identification of miRNAs involved in DRG neurite outgrowth and their
704 putative targets. *FEBS Lett* 2017; **591**:2091-2105.
705 19 Song Y, Ori-McKenney KM, Zheng Y, Han C, Jan LY, Jan YN. Regeneration of Drosophila sensory neuron
706 axons and dendrites is regulated by the Akt pathway involving Pten and microRNA bantam. *Genes Dev* 2012;
707 **26**:1612-1625.
708 20 Weng YL, An R, Cassin J *et al.* An Intrinsic Epigenetic Barrier for Functional Axon Regeneration. *Neuron* 2017;
709 **94**:337-346 e336.
710 21 Iskandar BJ, Rizk E, Meier B *et al.* Folate regulation of axonal regeneration in the rodent central nervous
711 system through DNA methylation. *J Clin Invest* 2010; **120**:1603-1616.

712 22 Loh YE, Koemeter-Cox A, Finelli MJ, Shen L, Friedel RH, Zou H. Comprehensive mapping of 5-
713 hydroxymethylcytosine epigenetic dynamics in axon regeneration. *Epigenetics* 2017; **12**:77-92.
714 23 Gaub P, Joshi Y, Wuttke A *et al.* The histone acetyltransferase p300 promotes intrinsic axonal regeneration.
715 *Brain* 2011; **134**:2134-2148.
716 24 Cho Y, Sloutsky R, Naegle KM, Cavalli V. Injury-induced HDAC5 nuclear export is essential for axon
717 regeneration. *Cell* 2013; **155**:894-908.
718 25 Finelli MJ, Wong JK, Zou H. Epigenetic regulation of sensory axon regeneration after spinal cord injury. *J*
719 *Neurosci* 2013; **33**:19664-19676.
720 26 Puttagunta R, Tedeschi A, Soria MG *et al.* PCAF-dependent epigenetic changes promote axonal
721 regeneration in the central nervous system. *Nat Commun* 2014; **5**:3527.
722 27 Palmisano I, Danzi MC, Hutson TH *et al.* Epigenomic signatures underpin the axonal regenerative ability of
723 dorsal root ganglia sensory neurons. *Nat Neurosci* 2019; **22**:1913-1924.
724 28 Lan F, Bayliss PE, Rinn JL *et al.* A histone H3 lysine 27 demethylase regulates animal posterior development.
725 *Nature* 2007; **449**:689-694.
726 29 Agger K, Cloos PA, Christensen J *et al.* UTX and JMJD3 are histone H3K27 demethylases involved in HOX
727 gene regulation and development. *Nature* 2007; **449**:731-734.
728 30 Welstead GG, Creyghton MP, Bilodeau S *et al.* X-linked H3K27me3 demethylase Utx is required for
729 embryonic development in a sex-specific manner. *Proc Natl Acad Sci U S A* 2012; **109**:13004-13009.
730 31 Yang X, Xu B, Mulvey B *et al.* Differentiation of human pluripotent stem cells into neurons or cortical
731 organoids requires transcriptional co-regulation by UTX and 53BP1. *Nat Neurosci* 2019; **22**:362-373.
732 32 Shan Y, Zhang Y, Zhao Y *et al.* JMJD3 and UTX determine fidelity and lineage specification of human neural
733 progenitor cells. *Nat Commun* 2020; **11**:382.
734 33 Pediconi N, Salerno D, Lupacchini L *et al.* EZH2, JMJD3, and UTX epigenetically regulate hepatic plasticity
735 inducing retro-differentiation and proliferation of liver cells. *Cell Death Dis* 2019; **10**:518.
736 34 Cuyas E, Verdura S, Llorach-Pares L *et al.* Metformin directly targets the H3K27me3 demethylase
737 KDM6A/UTX. *Aging Cell* 2018; **17**:e12772.
738 35 Jin C, Li J, Green CD *et al.* Histone demethylase UTX-1 regulates C. elegans life span by targeting the
739 insulin/IGF-1 signaling pathway. *Cell Metab* 2011; **14**:161-172.
740 36 Lin TY, Cheng YC, Yang HC *et al.* Loss of the candidate tumor suppressor BTG3 triggers acute cellular
741 senescence via the ERK-JMJD3-p16(INK4a) signaling axis. *Oncogene* 2012; **31**:3287-3297.
742 37 Agger K, Cloos PA, Rudkjaer L *et al.* The H3K27me3 demethylase JMJD3 contributes to the activation of the
743 INK4A-ARF locus in response to oncogene- and stress-induced senescence. *Genes Dev* 2009; **23**:1171-1176.
744 38 Mansour AA, Gafni O, Weinberger L *et al.* The H3K27 demethylase Utx regulates somatic and germ cell
745 epigenetic reprogramming. *Nature* 2012; **488**:409-413.
746 39 Zhao W, Li Q, Ayers S *et al.* Jmjd3 inhibits reprogramming by upregulating expression of INK4a/Arf and
747 targeting PHF20 for ubiquitination. *Cell* 2013; **152**:1037-1050.
748 40 Li X, Zhang Q, Shi Q *et al.* Demethylase Kdm6a epigenetically promotes IL-6 and IFN-beta production in
749 macrophages. *J Autoimmun* 2017; **80**:85-94.
750 41 Salminen A, Kaarniranta K, Hiltunen M, Kauppinen A. Histone demethylase Jumonji D3 (JMJD3/KDM6B) at
751 the nexus of epigenetic regulation of inflammation and the aging process. *J Mol Med (Berl)* 2014; **92**:1035-
752 1043.
753 42 van Haaften G, Dalgliesh GL, Davies H *et al.* Somatic mutations of the histone H3K27 demethylase gene UTX
754 in human cancer. *Nat Genet* 2009; **41**:521-523.

755 43 Yamamoto K, Tateishi K, Kudo Y *et al.* Loss of histone demethylase KDM6B enhances aggressiveness of
756 pancreatic cancer through downregulation of C/EBPalpha. *Carcinogenesis* 2014; **35**:2404-2414.
757 44 Tang Y, Li T, Li J *et al.* Jmjd3 is essential for the epigenetic modulation of microglia phenotypes in the
758 immune pathogenesis of Parkinson's disease. *Cell Death Differ* 2014; **21**:369-380.
759 45 Song W, Zsindely N, Farago A, Marsh JL, Bodai L. Systematic genetic interaction studies identify histone
760 demethylase Utx as potential target for ameliorating Huntington's disease. *Hum Mol Genet* 2018; **27**:649-666.
761 46 Tang GB, Zeng YQ, Liu PP *et al.* The Histone H3K27 Demethylase UTX Regulates Synaptic Plasticity and
762 Cognitive Behaviors in Mice. *Front Mol Neurosci* 2017; **10**:267.
763 47 Wijayatunge R, Liu F, Shpargel KB *et al.* The histone demethylase Kdm6b regulates a mature gene
764 expression program in differentiating cerebellar granule neurons. *Mol Cell Neurosci* 2018; **87**:4-17.
765 48 Wijayatunge R, Chen LF, Cha YM, Zannas AS, Frank CL, West AE. The histone lysine demethylase Kdm6b is
766 required for activity-dependent preconditioning of hippocampal neuronal survival. *Mol Cell Neurosci* 2014;
767 **61**:187-200.
768 49 Zhang M, Zhang Y, Xu Q *et al.* Neuronal Histone Methyltransferase EZH2 Regulates Neuronal
769 Morphogenesis, Synaptic Plasticity, and Cognitive Behavior in Mice. *Neurosci Bull* 2023.
770 50 Wang X-W, Yang S-G, Hu M-W *et al.* Histone methyltransferase Ezh2 coordinates mammalian axon
771 regeneration via epigenetic regulation of key regenerative pathways. *bioRxiv* 2022:488817.
772 51 Saijilafu, Hur EM, Zhou FQ. Genetic dissection of axon regeneration via in vivo electroporation of adult
773 mouse sensory neurons. *Nat Commun* 2011; **2**:543.
774 52 Tran NM, Shekhar K, Whitney IE *et al.* Single-Cell Profiles of Retinal Ganglion Cells Differing in Resilience to
775 Injury Reveal Neuroprotective Genes. *Neuron* 2019; **104**:1039-1055 e1012.
776 53 Wang XW, Yang SG, Zhang C *et al.* Knocking Out Non-muscle Myosin II in Retinal Ganglion Cells Promotes
777 Long-Distance Optic Nerve Regeneration. *Cell Rep* 2020; **31**:107537.
778 54 Walport LJ, Hopkinson RJ, Vollmar M *et al.* Human UTY(KDM6C) is a male-specific N-methyl lysyl
779 demethylase. *J Biol Chem* 2014; **289**:18302-18313.
780 55 Wang C, Lee JE, Cho YW *et al.* UTX regulates mesoderm differentiation of embryonic stem cells independent
781 of H3K27 demethylase activity. *Proc Natl Acad Sci U S A* 2012; **109**:15324-15329.
782 56 Kruidenier L, Chung CW, Cheng Z *et al.* A selective jumonji H3K27 demethylase inhibitor modulates the
783 proinflammatory macrophage response. *Nature* 2012; **488**:404-408.
784 57 Park KK, Liu K, Hu Y *et al.* Promoting axon regeneration in the adult CNS by modulation of the PTEN/mTOR
785 pathway. *Science* 2008; **322**:963-966.
786 58 Yang SG, Wang XW, Qian C, Zhou FQ. Reprogramming neurons for regeneration: The fountain of youth.
787 *Prog Neurobiol* 2022; **214**:102284.
788 59 Wilson C, Giono LE, Rozes-Salvador V, Fiszbein A, Kornblihtt AR, Caceres A. The Histone Methyltransferase
789 G9a Controls Axon Growth by Targeting the RhoA Signaling Pathway. *Cell Rep* 2020; **31**:107639.
790 60 Barnes AP, Lilley BN, Pan YA *et al.* LKB1 and SAD kinases define a pathway required for the polarization of
791 cortical neurons. *Cell* 2007; **129**:549-563.
792 61 Romaus-Sanjurjo D, Saikia JM, Kim HJ, Tsai KM, Le GQ, Zheng B. Overexpressing eukaryotic elongation factor
793 1 alpha (eEF1A) proteins to promote corticospinal axon repair after injury. *Cell Death Discov* 2022; **8**:390.
794 62 Wang PY, Seabold GK, Wenthold RJ. Synaptic adhesion-like molecules (SALMs) promote neurite outgrowth.
795 *Mol Cell Neurosci* 2008; **39**:83-94.
796 63 Qin S, Zou Y, Zhang CL. Cross-talk between KLF4 and STAT3 regulates axon regeneration. *Nat Commun* 2013;
797 **4**:2633.

798 64 Bray ER, Yungher BJ, Levay K *et al.* Thrombospondin-1 Mediates Axon Regeneration in Retinal Ganglion
799 Cells. *Neuron* 2019; **103**:642-657 e647.
800 65 Guo X, Zhou J, Starr C *et al.* Preservation of vision after CaMKII-mediated protection of retinal ganglion cells.
801 *Cell* 2021; **184**:4299-4314 e4212.
802 66 Yoo AS, Sun AX, Li L *et al.* MicroRNA-mediated conversion of human fibroblasts to neurons. *Nature* 2011;
803 **476**:228-231.
804 67 Sanuki R, Onishi A, Koike C *et al.* miR-124a is required for hippocampal axogenesis and retinal cone survival
805 through Lhx2 suppression. *Nat Neurosci* 2011; **14**:1125-1134.
806 68 Gu X, Xu X, Jia C *et al.* Molecular Mechanisms Involved in the Regulation of Neurodevelopment by miR-124.
807 *Mol Neurobiol* 2023; **60**:3569-3583.
808 69 Hong S, Cho YW, Yu LR, Yu H, Veenstra TD, Ge K. Identification of JmjC domain-containing UTX and JMJD3
809 as histone H3 lysine 27 demethylases. *Proc Natl Acad Sci U S A* 2007; **104**:18439-18444.
810 70 Burgold T, Spreafico F, De Santa F *et al.* The histone H3 lysine 27-specific demethylase Jmjd3 is required for
811 neural commitment. *PLoS One* 2008; **3**:e3034.
812 71 Naruse C, Shibata S, Tamura M *et al.* New insights into the role of Jmjd3 and Utx in axial skeletal formation
813 in mice. *FASEB J* 2017; **31**:2252-2266.
814 72 Yang L, Song LS, Liu XF *et al.* The Maternal Effect Genes UTX and JMJD3 Play Contrasting Roles in Mus
815 musculus Preimplantation Embryo Development. *Sci Rep* 2016; **6**:26711.
816 73 Shahhoseini M, Taghizadeh Z, Hatami M, Baharvand H. Retinoic acid dependent histone 3 demethylation
817 of the clustered HOX genes during neural differentiation of human embryonic stem cells. *Biochem Cell Biol*
818 2013; **91**:116-122.
819 74 Nakka K, Hachmer S, Mokhtari Z *et al.* JMJD3 activated hyaluronan synthesis drives muscle regeneration in
820 an inflammatory environment. *Science* 2022; **377**:666-669.
821 75 Guillermo ARR, Chocian K, Gavriilidis G *et al.* H3K27 modifiers regulate lifespan in C. elegans in a context-
822 dependent manner. *BMC Biol* 2021; **19**:59.
823 76 Kania AK, Price MJ, George-Alexander LE *et al.* H3K27me3 Demethylase UTX Restrains Plasma Cell
824 Formation. *J Immunol* 2022; **208**:1873-1885.
825 77 Ntziachristos P, Tsirigos A, Welstead GG *et al.* Contrasting roles of histone 3 lysine 27 demethylases in acute
826 lymphoblastic leukaemia. *Nature* 2014; **514**:513-517.
827 78 Van der Meulen J, Sanghvi V, Mavrakis K *et al.* The H3K27me3 demethylase UTX is a gender-specific tumor
828 suppressor in T-cell acute lymphoblastic leukemia. *Blood* 2015; **125**:13-21.
829 79 Zhang Y, Pang Y, Feng W *et al.* miR-124 regulates early isolation-induced social abnormalities via inhibiting
830 myelinogenesis in the medial prefrontal cortex. *Cell Mol Life Sci* 2022; **79**:507.
831 80 Papadimitriou E, Koutsoudaki PN, Thanou I *et al.* A miR-124-mediated post-transcriptional mechanism
832 controlling the cell fate switch of astrocytes to induced neurons. *Stem Cell Reports* 2023; **18**:915-935.
833 81 Cates K, McCoy MJ, Kwon JS *et al.* Deconstructing Stepwise Fate Conversion of Human Fibroblasts to
834 Neurons by MicroRNAs. *Cell Stem Cell* 2021; **28**:127-140 e129.
835 82 Davis EJ, Broestl L, Abdulai-Saiku S *et al.* A second X chromosome contributes to resilience in a mouse model
836 of Alzheimer's disease. *Sci Transl Med* 2020; **12**.
837 83 Quigley HA, Broman AT. The number of people with glaucoma worldwide in 2010 and 2020. *Br J Ophthalmol*
838 2006; **90**:262-267.
839 84 Chiu SL, Chu CL, Muo CH, Chen CL, Lan SJ. The Prevalence and the Incidence of Diagnosed Open-Angle
840 Glaucoma and Diagnosed Angle-Closure Glaucoma: Changes From 2001 to 2010. *J Glaucoma* 2016; **25**:e514-
841 519.

842 85 Luo X, Salgueiro Y, Beckerman SR, Lemmon VP, Tsoulfas P, Park KK. Three-dimensional evaluation of retinal
843 ganglion cell axon regeneration and pathfinding in whole mouse tissue after injury. *Exp Neurol* 2013; **247**:653-
844 662.
845 86 Erturk A, Hellal F, Enes J, Bradke F. Disorganized microtubules underlie the formation of retraction bulbs
846 and the failure of axonal regeneration. *J Neurosci* 2007; **27**:9169-9180.

Figure 1

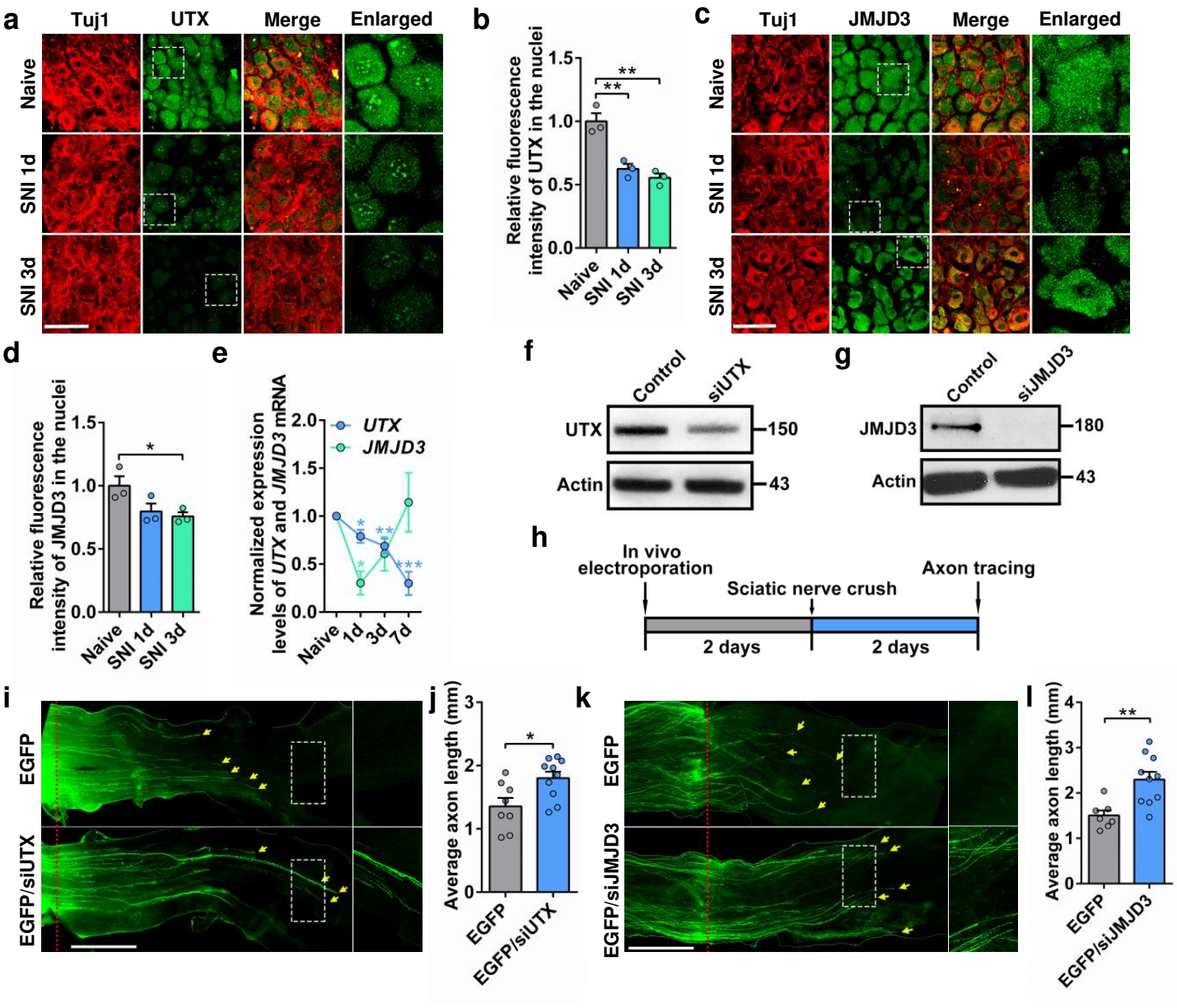
a
Tuj1
UTX
Merge
Enlarged
Naive
SNI 1d
SNI 3d
b
Relative fluorescence intensity of UTX in the nuclei
1.5
1.0
0.5
0.0
**
**
Naive
SNI 1d
SNI 3d
c
Tuj1
JMJD3
Merge
Enlarged
Naive
SNI 1d
SNI 3d
d
Relative fluorescence intensity of JMJD3 in the nuclei
1.5
1.0
0.5
0.0
*
Naive
SNI 1d
SNI 3d
e
Normalized expression levels of UTX and JMJD3 mRNA
UTX
JMJD3
2.0
1.5
1.0
0.5
0.0
Naive
1d
3d
7d
f
Control
siUTX
UTX
150
Actin
43
g
Control
siJMJD3
JMJD3
180
Actin
43
h
In vivo electroporation
Sciatic nerve crush
Axon tracing
2 days
2 days
i
EGFP
EGFP/siUTX
j
Average axon length (mm)
3
2
1
0
*
EGFP
EGFP/siUTX
k
EGFP
EGFP/siJMJD3
l
Average axon length (mm)
4
3
2
1
0
**
EGFP
EGFP/siJMJD3

Fig. 1 | Knocking down *UTX* or *JMJD3* in adult mouse sensory neurons markedly enhanced sensory axon regeneration in vivo.

(a) Immunostaining of DRG sections showing significantly reduced level of UTX in adult mouse sensory neurons in vivo after sciatic nerve injury (SNI). The 4th column shows enlarged images of areas indicated by the dashed white boxes in the 2nd column. Images were stained for neuronal marker Tuj1 (red) and UTX (green). Scale bar, 100 µm for the first 3 columns and 30 µm for the 4th column.

(b) Quantification of relative fluorescence intensity of UTX immunostaining shown in (a) (one way ANOVA followed by Tukey's multiple comparison test, P=0.0012; n=3 independent experiments for each condition).

(c) Immunostaining of DRG sections showing significantly reduced level of JMJD3 in adult mouse sensory neurons in vivo at day 1 after sciatic nerve injury (SNI). The 4th column shows enlarged images of areas indicated by the dashed white boxes in the 2nd column. Images were stained for neuronal marker Tuj1 (red) and JMJD3 (green). Scale bar, 100 µm for the first 3 columns and 30 µm for the 4th column.

(d) Quantification of relative fluorescence intensity of JMJD3 immunostaining shown in (c) (two tailed student's t tests, P=0.0426; n=3 independent experiments for each condition).

(e) Time course of expression of *UTX* and *JMJD3* transcripts in ipsilateral L4/L5 DRG from naive mice and 1, 3, and 7 days post-sciatic nerve crush by real time PCR analysis. (one way ANOVA followed by Tukey's multiple comparison test, *UTX*: P=0.0001, n=5 independent experiments for each condition; *JMJD3*: P=0.0165, n=7 independent experiments for each condition).

(f) Western blot image showing greatly reduced protein level of UTX in DRG tissues 2 days after in vivo electroporation of siRNAs against *UTX* (siUTX). A representative image from 2 independent experiments is shown.

(g) Western blot image showing greatly reduced protein level of JMJD3 in DRG tissues 2 days after in vivo electroporation of siRNAs against *JMJD3* (siJMJD3). A representative image from 2 independent experiments is shown.

(h) Schematics of in vivo electroporation and investigation of axon regeneration after knocking down *UTX* or *JMJD3*. L4 and L5 DRGs of wild type adult mice were electroporated in vivo with EGFP or EGFP + siRNAs against *UTX* (siUTX) or *JMJD3* (siJMJD3). To assess the promoting effects, axon regeneration analyses were performed 2 days post-sciatic nerve crush, when sensory axon regeneration has not reached its optimal rate.

(i) Representative images of in vivo sensory axon regeneration in mice electroporated with either EGFP or EGFP+siUTX. The right column shows enlarged images of areas indicated by the dashed white boxes in the left column. The red dotted lines indicate the nerve crush sites. Yellow arrows indicate the distal ends of regenerating axons. Scale bar, 1 mm for the left column and 0.5 mm for the right column.

(j) Knocking down *UTX* in sensory neurons significantly promoted sensory axon regeneration in vivo (two tailed student's *t* tests, P=0.0152; EGFP; n= 8 mice, EGFP+siUTX; n= 10 mice).

(k) Representative images of in vivo sensory axon regeneration in mice electroporated with either EGFP or EGFP+siJMJD3. The right column shows enlarged images of areas indicated by the dashed white boxes in the left column. The red dotted lines indicate the nerve crush sites. Yellow arrows indicate the distal ends of regenerating axons. Scale bar, 1 mm for the left column and 0.5 mm for the right column.

(l) Knocking down *JMJD3* in sensory neurons significantly promoted sensory axon regeneration in vivo (two tailed student's t tests, P=0.0033; EGFP: n=7 mice, EGFP+siJMJD3: n=10 mice).

*, **, ***$P < 0.05$, 0.01, 0.001, respectively. Data are represented as mean ± SEM.

Figure 2

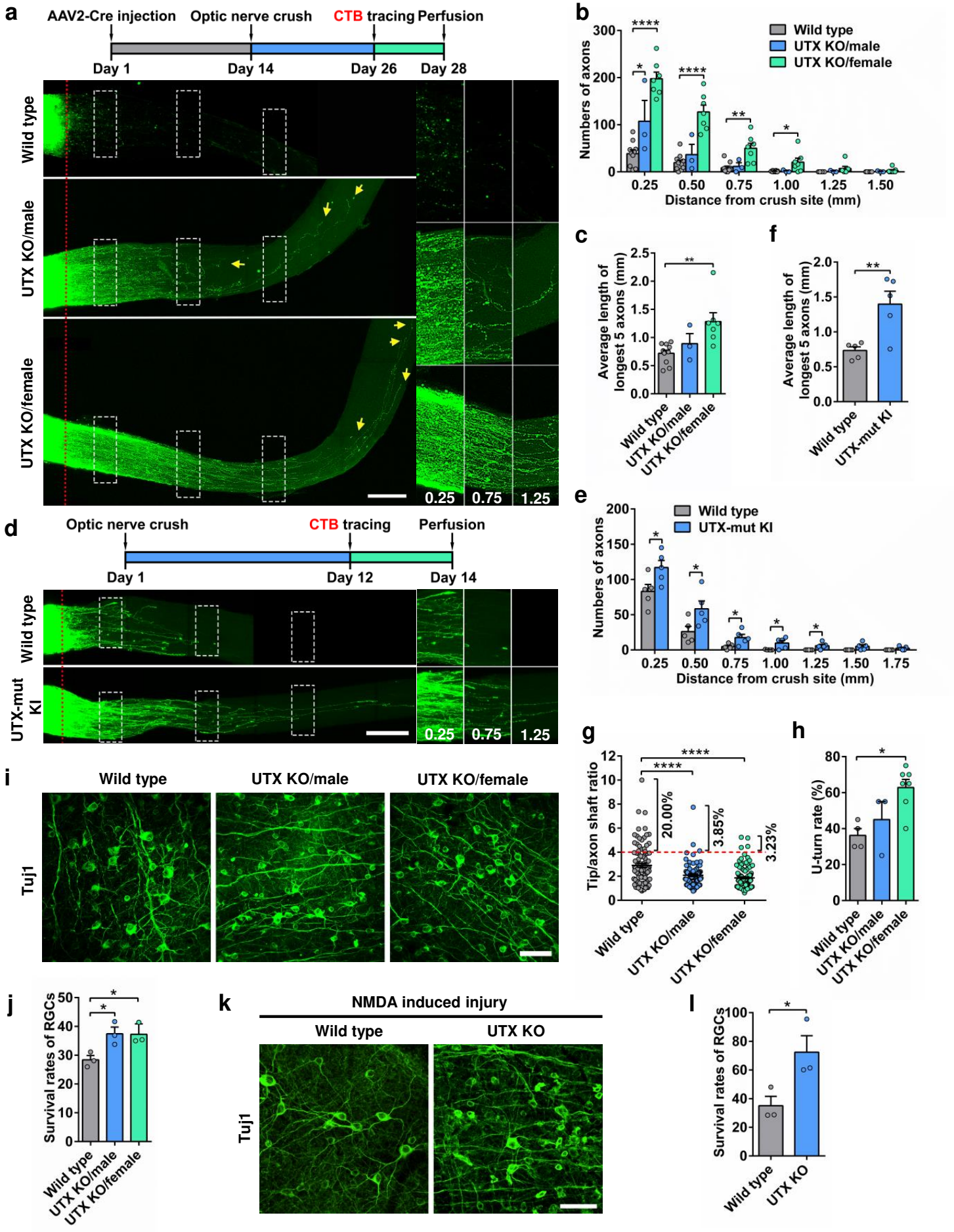
a
AAV2-Cre injection
Optic nerve crush
CTB tracing
Perfusion
Day 1
Day 14
Day 26
Day 28
Wild type
UTX KO/male
UTX KO/female
0.25
0.75
1.25
b
Numbers of axons
Wild type
UTX KO/male
UTX KO/female
Distance from crush site (mm)
c
Average length of longest 5 axons (mm)
Wild type
UTX KO/male
UTX KO/female
f
Average length of longest 5 axons (mm)
Wild type
UTX-mut KI
d
Optic nerve crush
CTB tracing
Perfusion
Day 1
Day 12
Day 14
Wild type
UTX-mut KI
e
Numbers of axons
Wild type
UTX-mut KI
Distance from crush site (mm)
g
Tip/axon shaft ratio
20.00%
3.85%
3.23%
h
U-turn rate (%)
i
Wild type
UTX KO/male
UTX KO/female
Tuj1
j
Survival rates of RGCs
k
NMDA induced injury
Wild type
UTX KO
Tuj1
l
Survival rates of RGCs

Fig. 2 | Conditional deletion of H3K27 demethylase UTX in mouse retinal ganglion cells (RGCs) markedly promoted optic nerve regeneration and RGC survival.

(a) Top: schematic time course of optic nerve regeneration model. Specifically, AAV2-Cre was injected at day 1 and the optic nerve was crushed 2 weeks later. Optic nerve regeneration was analyzed 2 weeks after the nerve crush, and the fluorescence (Alexa 594) tagged cholera toxin β subunit (CTB) was injected 2 days before collecting the optic nerve. Bottom: representative 2D projected confocal images of whole mount cleared optic nerves of wild type, male *UTX* knockout (UTX KO/male), female *UTX* knockout (UTX KO/female) mice 2 weeks after optic nerve crush (ONC). The regenerating axons were labeled with CTB-Alexa 594. Yellow arrows indicate the distal ends of regenerating axons. The red dotted lines indicate the nerve crush sites. The columns on the right display magnified images of the areas in white, dashed boxes on the left, showing axons at 0.25, 0.75, and 1.25 mm distal to the crush sites. Scale bar, 200 µm for the left column and 100 µm for the magnified images.

(b) Quantification of regenerating axons at different distances distal to the nerve crush site (0.25 to 1.50 mm) (one way ANOVA followed by Tukey's multiple comparisons test, $P<0.0001$; wild type: n=10 mice, UTX KO/male: n=3 mice, UTX KO/female: n=7).

(c) Quantification of the average length of the top 5 longest axons of each nerve in (a) (one way ANOVA followed by Tukey's multiple comparisons test, P=0.0052; wild type: n=10 mice, UTX KO/male: n=3 mice, UTX KO/female: n=7).

(d)Top: schematic time course of optic nerve regeneration model. Optic nerve regeneration was analyzed 2 weeks after the nerve crush, and the fluorescence (Alexa 594) tagged CTB was injected 2 days before collecting the optic nerve. Bottom: representative 2D projected confocal images of whole mount cleared optic nerves of *UTX* mutant knockin (UTX-mut KI) and wild type mice 2 weeks after ONC. The regenerating axons were labeled with CTB-Alexa 594. The red dotted lines indicate the nerve crush sites. The columns on the right display magnified images of the areas in white, dashed boxes on the left, showing axons at 0.25, 0.75, and 1.25 mm distal to the crush sites. Scale bar, 200 µm for the left column and 150 µm for the magnified images.

(e) Quantification of regenerating axons at different distances distal to the nerve crush site (0.25 to 1.75 mm) in UTX-mut KI and wild type mice after ONC. Bar graph showing robust optic nerve regeneration in UTX-mut KI mice (two tailed student's t tests, P<0.05; Wild type: n=5 mice, UTX-mut KI: n=5 mice).

(f) Quantification of the average length of the top 5 longest axons of each nerve in (d) (two tailed student's t tests, P=0.0087; Wild type: n=5 mice, UTX-mut KI: n=5 mice).

(g) Quantification of the size of retraction bulbs and growth cones by tip/axon shaft ratio in Extended Data Fig. 3 (one way ANOVA followed by Tukey's multiple comparisons test, $P<0.0001$; n=105, 78, and 124 axons pooled from 7 mice for wild type, 3 mice for UTX KO/male, and 7 mice for UTX KO/female, respectively).

(h) Quantification of U-turn rate in Extended Data Fig. 3 (one way ANOVA followed by Tukey's multiple comparisons test, $P=0.0126$; wild type: n=4 mice, UTX KO/male: n=3 mice, UTX KO/female: n=7; top 20 longest axons were analyzed for each mouse).

(i) Representative images of flat whole mount retina immunostained for neuronal marker Tuj1 (green), indicating increased RGC survival rates in either male *UTX* knockout (UTX KO/male) or female *UTX* knockout (UTX KO/female) mice compared with that in wild type mice. Scale bar, 50 µm.

(j) Quantification of RGC survival rates in wild type, male *UTX* knockout or female *UTX* knockout mice after ONC (one way ANOVA followed by Tukey's multiple comparisons test, $P=0.0291$; n=3 mice for each condition).

(k) Representative images of flat whole mount retina immunostained for neuronal marker Tuj1 (red), indicating increased RGC survival rates in *UTX* knockout (UTX KO) mice compared with that in wild type mice after NMDA induced injury. Scale bar, 50 µm.

(l) Quantification of RGC survival rate in (k) (two tailed student's t tests, P=0.0485; n=3 mice for each condition).

*, **, ***, ****$P < 0.05$, 0.01, 0.001, 0.0001, respectively. Data are represented as mean ± SEM. See also Extended Data Figs. 1–6.

Figure 3

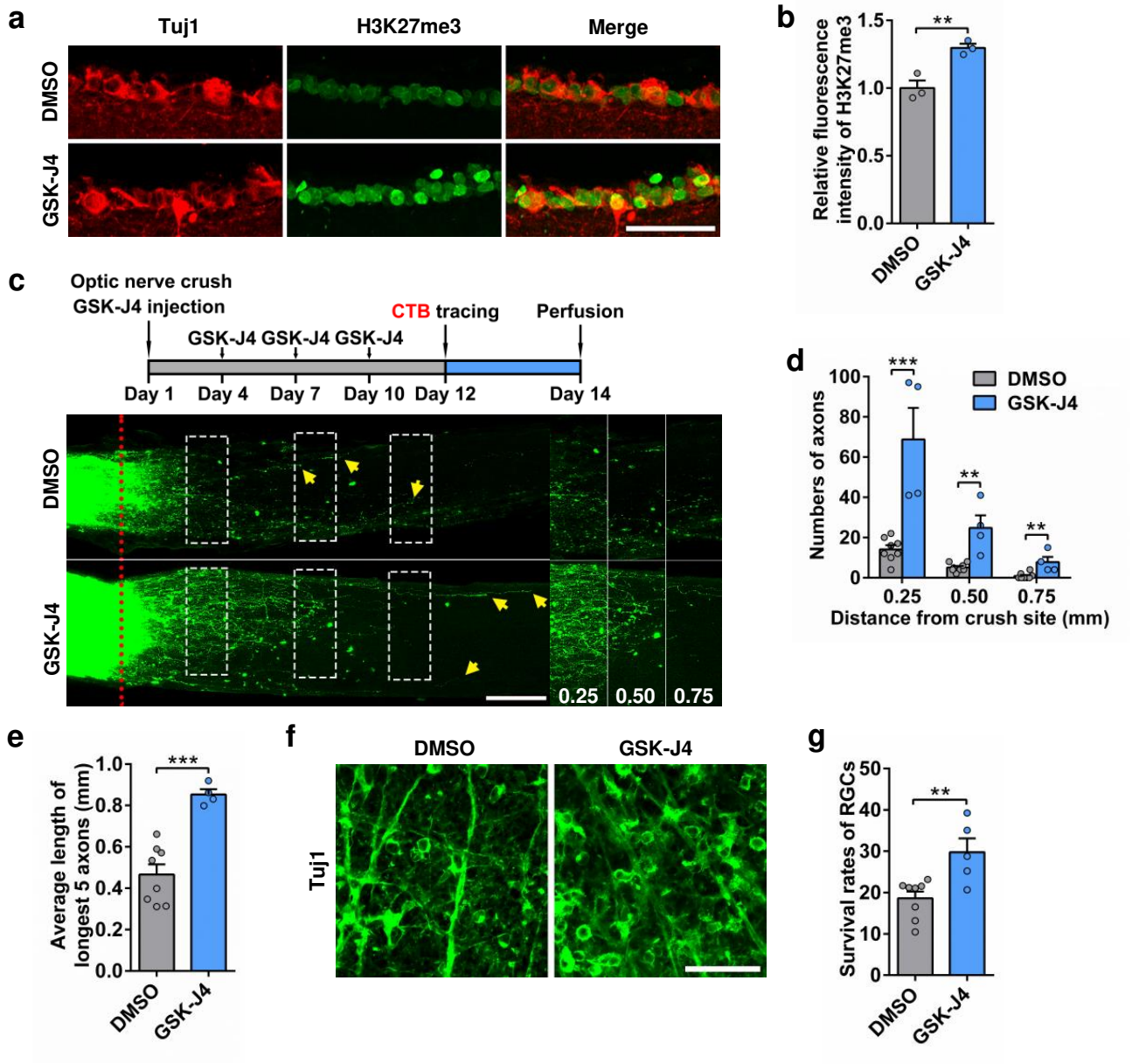
a
Tuj1
H3K27me3
Merge
DMSO
GSK-J4
b
Relative fluorescence intensity of H3K27me3
1.5
1.0
0.5
0.0
**
DMSO
GSK-J4
c
Optic nerve crush
GSK-J4 injection
CTB tracing
Perfusion
GSK-J4 GSK-J4 GSK-J4
Day 1
Day 4
Day 7
Day 10
Day 12
Day 14
DMSO
GSK-J4
0.25
0.50
0.75
d
Numbers of axons
100
80
60
40
20
0
***
**
**
DMSO
GSK-J4
0.25
0.50
0.75
Distance from crush site (mm)
e
Average length of longest 5 axons (mm)
1.0
0.8
0.6
0.4
0.2
0.0
***
DMSO
GSK-J4
f
DMSO
GSK-J4
Tuj1
g
Survival rates of RGCs
50
40
30
20
10
0
**
DMSO
GSK-J4

Fig. 3 | Pharmacological delayed inhibition of UTX in mouse retinal ganglion cells (RGCs) also promoted optic nerve regeneration and RGC survival.

(a) Confocal images of retinal sections from wild type mice injected with UTX/JMJD3 inhibitor GSK-J4 or DMSO (as control) showing significantly increased level of H3K27me3 in RGCs by blockade of histone demethylases activity. The sections were stained for neuronal marker Tuj1 (red), which labeled RGCs, and H3K27me3 (green). Scale bar, 50 µm.

(b) Quantification of relative fluorescence intensity of H3K27me3 immunostaining shown in (a) (two tailed student's *t* tests, P=0.0091; n=3 mice for each condition).

(c) Top: schematic time course of optic nerve regeneration model. Specifically, GSK-J4 or DMSO was injected once every 3 days for 4 times after ONC. Optic nerve regeneration was analyzed 2 weeks after the nerve crush, and the fluorescence (Alexa 594) tagged CTB was injected 2 days before collecting the optic nerve. Bottom: representative 2D projected confocal images of whole mount cleared optic nerves of wild type mice with intravitreal injection of GSK-J4 or DMSO 2 weeks after ONC. The regenerating axons were labeled with CTB-Alexa 594. The red dotted lines indicate the nerve crush sites. The columns on the right display magnified images of the areas in white, dashed boxes on the left, showing axons at 0.25, 0.50, and 0.75 mm distal to the crush sites. Scale bar, 200 µm for the left column and 130 µm for the magnified images.

(d) Quantification of regenerating axons at different distances distal to the nerve crush site (0.25 to 0.75 mm) in injected GSK-J4 or DMSO mice after ONC. Bar graph showing robust optic nerve regeneration induced by GSK-J4 (two tailed student's *t* tests, P<0.01; DMSO: n=8 mice, GSK-J4: n=4 mice).

(e) Quantification of the average length of the top 5 longest axons of each nerve in (c) (two tailed student's *t* tests, P=0.0004; DMSO: n=8 mice, GSK-J4: n=4 mice).

(f) Representative images of flat whole mount retina immunostained for neuronal marker Tuj1 (green), indicating increased RGC survival rates in injected GSK-J4 mice compared with that in mice with DMSO injection. Scale bar, 50 µm.

(g) Quantification of RGC survival rate in (f) (two tailed student's t tests, P=0.0063; DMSO: n=8 mice, GSK-J4: n=5 mice).

*, **, ***, **** P < 0.05, 0.01, 0.001, 0.0001, respectively. Data are represented as mean ± SEM.

Figure 4

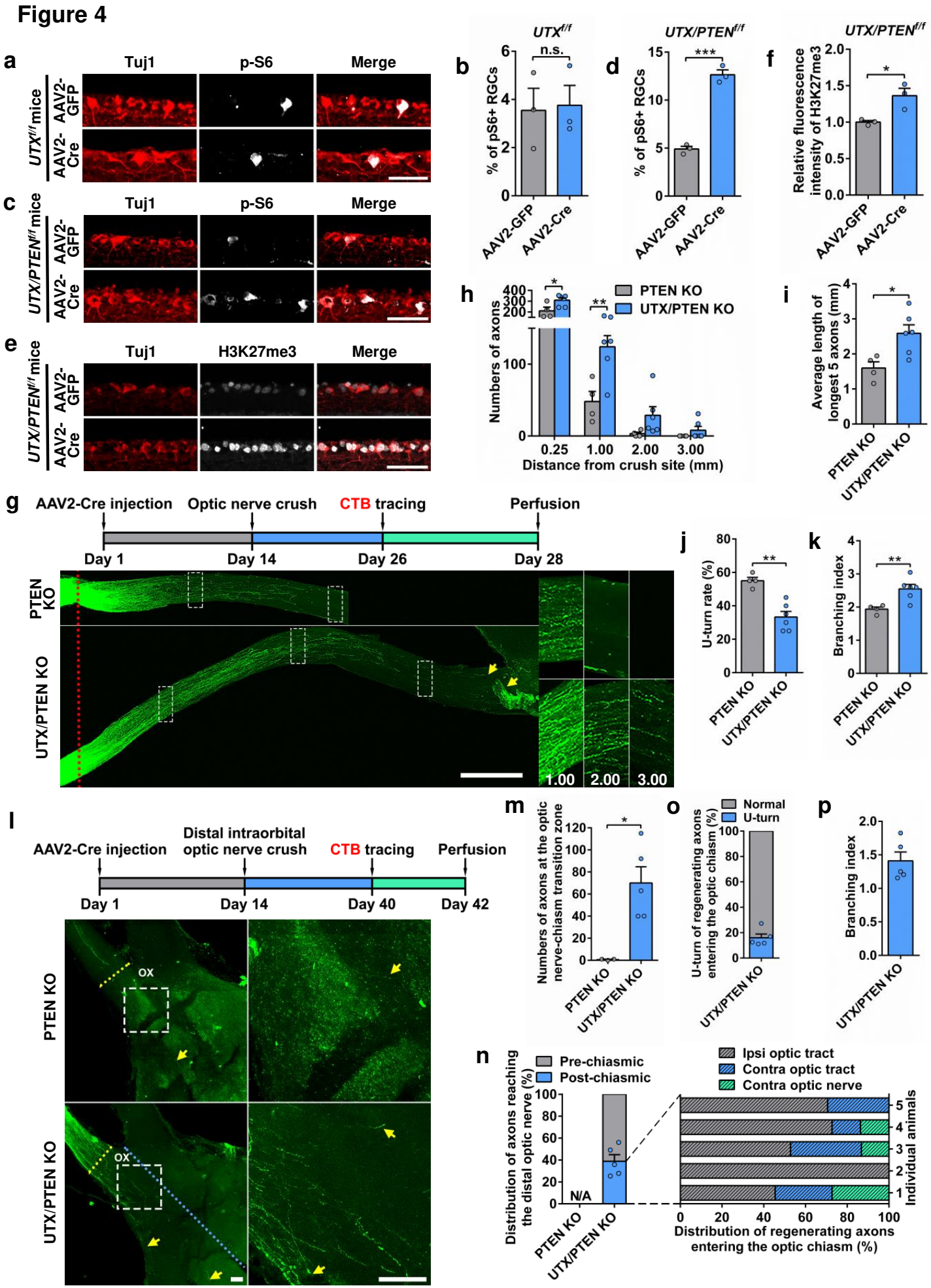
a
Tuj1
p-S6
Merge
UTX f/f mice
AAV2-GFP
AAV2-Cre
b
UTX f/f
n.s.
% of pS6+ RGCs
AAV2-GFP
AAV2-Cre
c
UTX/PTEN f/f mice
d
UTX/PTEN f/f
***
e
H3K27me3
f
Relative fluorescence intensity of H3K27me3
*
h
PTEN KO
UTX/PTEN KO
Numbers of axons
**
Distance from crush site (mm)
i
Average length of longest 5 axons (mm)
g
AAV2-Cre injection
Optic nerve crush
CTB tracing
Perfusion
Day 1
Day 14
Day 26
Day 28
1.00
2.00
3.00
j
U-turn rate (%)
k
Branching index
l
Distal intraorbital optic nerve crush
Day 40
Day 42
ox
m
Numbers of axons at the optic nerve-chiasm transition zone
o
Normal
U-turn
U-turn of regenerating axons entering the optic chiasm (%)
p
n
Pre-chiasmic
Post-chiasmic
Distribution of axons reaching the distal optic nerve (%)
N/A
Ipsi optic tract
Contra optic tract
Contra optic nerve
Individual animals
Distribution of regenerating axons entering the optic chiasm (%)

Fig. 4 | Synergistic promoting effects of *UTX* and *PTEN* double knockout on axon regeneration after ONC.

(a) Confocal images of retinal sections from *UTX*$^{f/f}$ mice injected with of AAV2-GFP or AAV2-Cre showing no effect of *UTX* single deletion on the percentage of p-S6+ RGCs the ganglion cell layer (GCL). The sections were stained for neuronal marker Tuj1 (red), which labeled RGCs, and p-S6 (gray). Scale bar, 50 µm.
(b) Quantification of p-S6+ RGCs in (a) (two tailed student's *t* tests, *P*=0.8747; n=3 mice for each condition).
(c) Confocal images of retinal sections from *UTX/PTEN*$^{f/f}$ mice injected with of AAV2-GFP or AAV2-Cre showing markedly increased percentage of p-S6+ RGCs the ganglion cell layer (GCL) via Cre-mediated double deletion. The sections were stained for neuronal marker Tuj1 (red), which labeled RGCs, and p-S6 (gray). Scale bar, 50 µm.
(d) Quantification of p-S6+ RGCs in (c) (two tailed student's *t* tests, *P*=0.0002; n=3 mice for each condition).
(e) Confocal images of retinal sections from *UTX/PTEN*$^{f/f}$ mice injected with of AAV2-GFP or AAV2-Cre showing significantly increased level of H3K27me3 in RGCs via Cre-mediated double deletion. The sections were stained for neuronal marker Tuj1 (red), which labeled RGCs, and H3K27me3 (gray). Scale bar, 50 µm.
(f) Quantification of relative fluorescence intensity of H3K27me3 immunostaining shown in (e) (two tailed student's *t* tests, *P*=0.0252; n=3 mice for each condition).
(g) Top: schematic time course of optic nerve regeneration model. Specifically, AAV2-Cre was injected at day 1 and the optic nerve was crushed 2 weeks later. Optic nerve regeneration was analyzed 2 weeks after the nerve crush, and the fluorescence (Alexa 594) tagged CTB was injected 2 days before collecting the optic nerve. Bottom: representative 2D projected confocal images of whole mount cleared optic nerves of *PTEN* knockout (PTEN KO) or *UTX*/*PTEN* double knockout (UTX/PTEN KO) mice 2 weeks after ONC. The regenerating axons were labeled with CTB-Alexa 594. Yellow arrows indicate the distal ends of regenerating axons. The red dotted lines indicate the nerve crush sites. OX indicates the optic chiasm. The columns on the right display magnified images of the areas in white, dashed boxes on the left, showing axons at 1.00, 2.00, and 3.00 mm distal to the crush sites. Scale bar, 500 µm for the left column and 250 µm for the magnified images.
(h) Quantification of regenerating axons at different distances distal to the nerve crush site (0.25 to 3.00 mm) in *PTEN* knockout (PTEN KO) or *UTX*/*PTEN* double knockout mice (UTX/PTEN KO) 2 weeks after ONC (two tailed student's *t* tests, *P*<0.05; PTEN KO: n=4 mice, UTX/PTEN KO: n=6 mice).
(i) Quantification of the average length of the top 5 longest axons of each nerve in (i) (two tailed student's *t* tests, *P*=0.0184; PTEN KO: n=4 mice, UTX/PTEN KO: n=6 mice).
(j) Quantification of U-turn rate in Extended Data Fig. 5b (two tailed student's *t* tests, *P*=0.0013; PTEN KO: n=4 mice, UTX/PTEN KO: n=6 mice; top 20 longest axons were analyzed for each mouse).
(k) Quantification of branching index by tip number/axon number (the top 20 longest axons) ratio in Extended Data Fig. 5b (two tailed student's *t* tests, *P*=0.0088; PTEN KO: n=4 mice, UTX/PTEN KO: n=6 mice).
(l) Top: schematic time course of optic nerve regeneration model. The optic nerve was crushed at the distal intraorbital site. Optic nerve regeneration was analyzed 4 weeks after the nerve crush. Bottom: Representative 2D projected confocal images of whole mount cleared optic chiasm areas of *PTEN* knockout (PTEN KO) or *UTX/PTEN* double knockout (UTX/PTEN KO) mice 4 weeks after distal intraorbital optic nerve crush. The right column shows enlarged images of areas indicated by the dashed white boxes in the left column. The regenerating axons at the optic chiasm were labeled with CTB-Alexa 594. Yellow arrows indicate the distal ends of regenerating axons. Blue and yellow dotted lines indicate the chiasm midline and the optic nerve-chiasm transition zone, respectively. OX indicates the optic chiasm. Scale bar, 100 µm.
(m) Quantification of regenerating axons reaching the optic chiasm in (l) (two tailed student's *t* tests, *P*=0.0125; PTEN KO: n=3 mice, UTX/PTEN KO: n=5 mice).
(n) Distribution of regenerating axons reaching the distal optic nerve (Pre-chiasmic) and entering the optic chiasm (Post-chiasmic) in (l). The dashed lines showing quantification of post-chiasmic axons projecting into the ipsilateral optic tract (Ipsi optic tract), contralateral optic tract (Contra optic tract), and contralateral optic nerve (Contra optic nerve) in 5 individual mice. N/A, not applicable.
(o) Quantification of U-turn rate in Extended Data Fig. 7 (n=5 mice; all axons into the optic chiasm were analyzed for each mouse).
(p) Quantification of branching index by tip number/axon number (regenerating axons into the optic chiasm) ratio in Extended Data Fig. 7 (n=5 mice).
n.s. $P > 0.05$; *, **, ***$P < 0.05$, 0.01, 0.001, respectively. Data are represented as mean ± SEM. See also Extended Data Figs. 7-9.

Figure 5

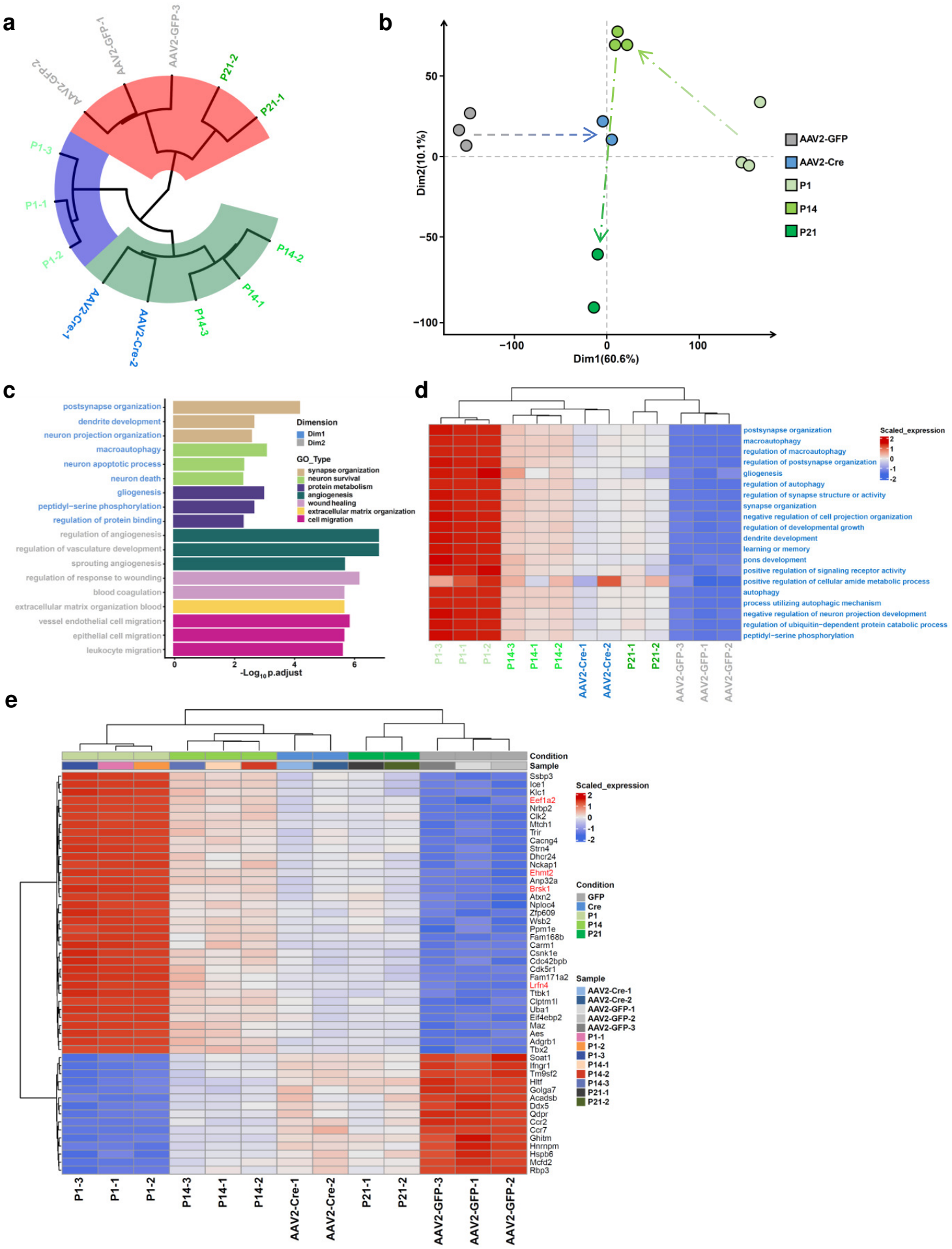
a
AAV2-GFP-1
AAV2-GFP-3
AAV2-GFP-2
P21-2
P21-1
P1-3
P1-1
P1-2
P14-2
P14-1
P14-3
AAV2-Cre-1
AAV2-Cre-2
b
Dim2(10.1%)
Dim1(60.6%)
AAV2-GFP
AAV2-Cre
P1
P14
P21
c
postsynapse organization
dendrite development
neuron projection organization
macroautophagy
neuron apoptotic process
neuron death
gliogenesis
peptidyl−serine phosphorylation
regulation of protein binding
regulation of angiogenesis
regulation of vasculature development
sprouting angiogenesis
regulation of response to wounding
blood coagulation
extracellular matrix organization blood
vessel endothelial cell migration
epithelial cell migration
leukocyte migration
Dimension
Dim1
Dim2
GO_Type
synapse organization
neuron survival
protein metabolism
angiogenesis
wound healing
extracellular matrix organization
cell migration
-Log10 p.adjust
d
Scaled_expression
postsynapse organization
macroautophagy
regulation of macroautophagy
regulation of postsynapse organization
gliogenesis
regulation of autophagy
regulation of synapse structure or activity
synapse organization
negative regulation of cell projection organization
regulation of developmental growth
dendrite development
learning or memory
pons development
positive regulation of signaling receptor activity
positive regulation of cellular amide metabolic process
autophagy
process utilizing autophagic mechanism
negative regulation of neuron projection development
regulation of ubiquitin−dependent protein catabolic process
peptidyl−serine phosphorylation
e
Condition
Sample
Scaled_expression
Condition
GFP
Cre
P1
P14
P21
Sample
AAV2-Cre-1
AAV2-Cre-2
AAV2-GFP-1
AAV2-GFP-2
AAV2-GFP-3
P1-1
P1-2
P1-3
P14-1
P14-2
P14-3
P21-1
P21-2

Fig. 5 | Deleting *UTX* switches the RGC transcriptomics into a developmental-like state.

(a) Hierarchical clustering based on Euclidean distance of all samples. Circular dendrogram shows two major clusters, while P1, P14 and UTX KO (AAV2-Cre) clustered together, P21 and wild type (AAV2-GFP) clustered separately.

(b) Principal component analysis (PCA) of transcriptomic profiles indicating the variation among all samples. Score plot shows a clear separation between P1, P14, P21, wild type (AAV2-Cre) and UTX KO (AAV2-GFP). The first two dimensions (Dim) accounted for 70.7% of variance. Note that Dim 1 predominantly reflects differences between wild type and UTX KO.

(c) Selected Gene Ontology (GO) terms were generated separately for Dim 1 and 2 genes (adjusted *P*-value < 0.05).

(d) Heatmap of top 20 enriched GO terms for Dim 1. The Color intensities indicate the z-score of genes contributing to each GO term.

(e) Heatmap showing scaled expression of top 50 genes for Dim 1.

See also Extended Data Figs. 10, 11.

Figure 6

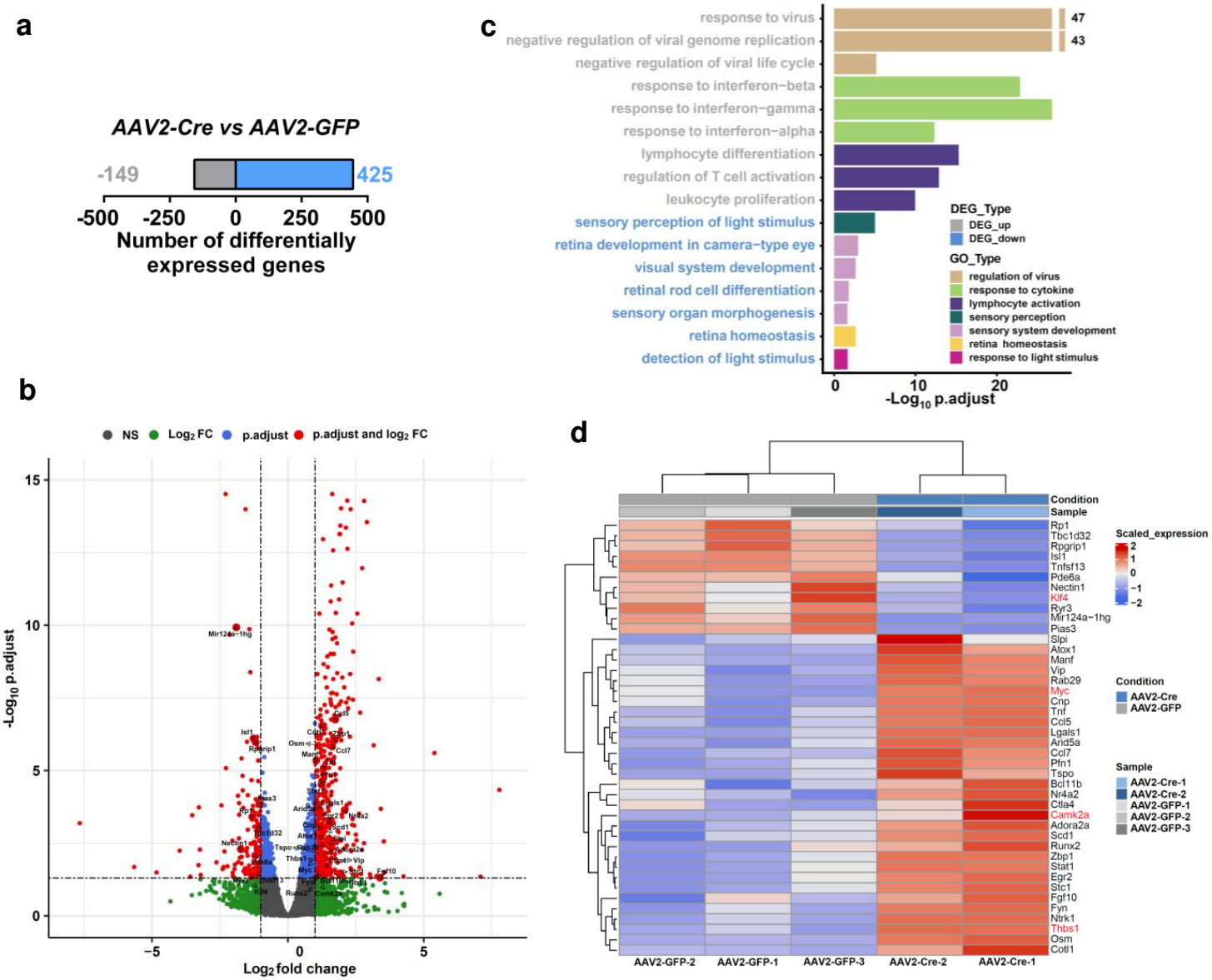
a
AAV2-Cre vs AAV2-GFP
-149
425
-500 -250 0 250 500
Number of differentially expressed genes
c
response to virus
negative regulation of viral genome replication
negative regulation of viral life cycle
response to interferon−beta
response to interferon−gamma
response to interferon−alpha
lymphocyte differentiation
regulation of T cell activation
leukocyte proliferation
sensory perception of light stimulus
retina development in camera−type eye
visual system development
retinal rod cell differentiation
sensory organ morphogenesis
retina homeostasis
detection of light stimulus
47
43
DEG_Type
DEG_up
DEG_down
GO_Type
regulation of virus
response to cytokine
lymphocyte activation
sensory perception
sensory system development
retina homeostasis
response to light stimulus
0 10 20
-Log10 p.adjust
b
NS
Log2 FC
p.adjust
p.adjust and log2 FC
-Log10 p.adjust
Log2 fold change
d
Condition
Sample
Scaled_expression
Condition
AAV2-Cre
AAV2-GFP
Sample
AAV2-Cre-1
AAV2-Cre-2
AAV2-GFP-1
AAV2-GFP-2
AAV2-GFP-3
AAV2-GFP-2
AAV2-GFP-1
AAV2-GFP-3
AAV2-Cre-2
AAV2-Cre-1

Fig. 6 | Deleting *UTX* induces changes of the RGC transcriptomics with roles in sensory system development, axon growth, and other functions.

(a) Number of differentially expressed genes between wild type (AAV2-GFP) and UTX KO (AAV2-Cre) at the threshold of adjusted *P*-value < 0.05.

(b) Volcano plot showing differential gene expression between wild type (AAV2-GFP) and UTX KO (AAV2-Cre) RGCs. Positive $\log_2$ fold change indicates higher expression in UTX KO RGCs relative to wild type RGCs. Red points indicate that genes are considered significantly different if absolute $\log_2$ Fold change > 1 and adjusted *P*-value < 0.05; vertical and horizontal reference lines at respective values.

(c) Selected Gene Ontology (GO) terms were generated separately for genes upregulated or downregulated (adjusted *P*-value < 0.05) by UTX KO RGCs relative to wild type RGCs.

(d) Heatmap of selected genes relevant to axon regeneration.

See also Extended Data Figs. 10, 11.

Figure 7

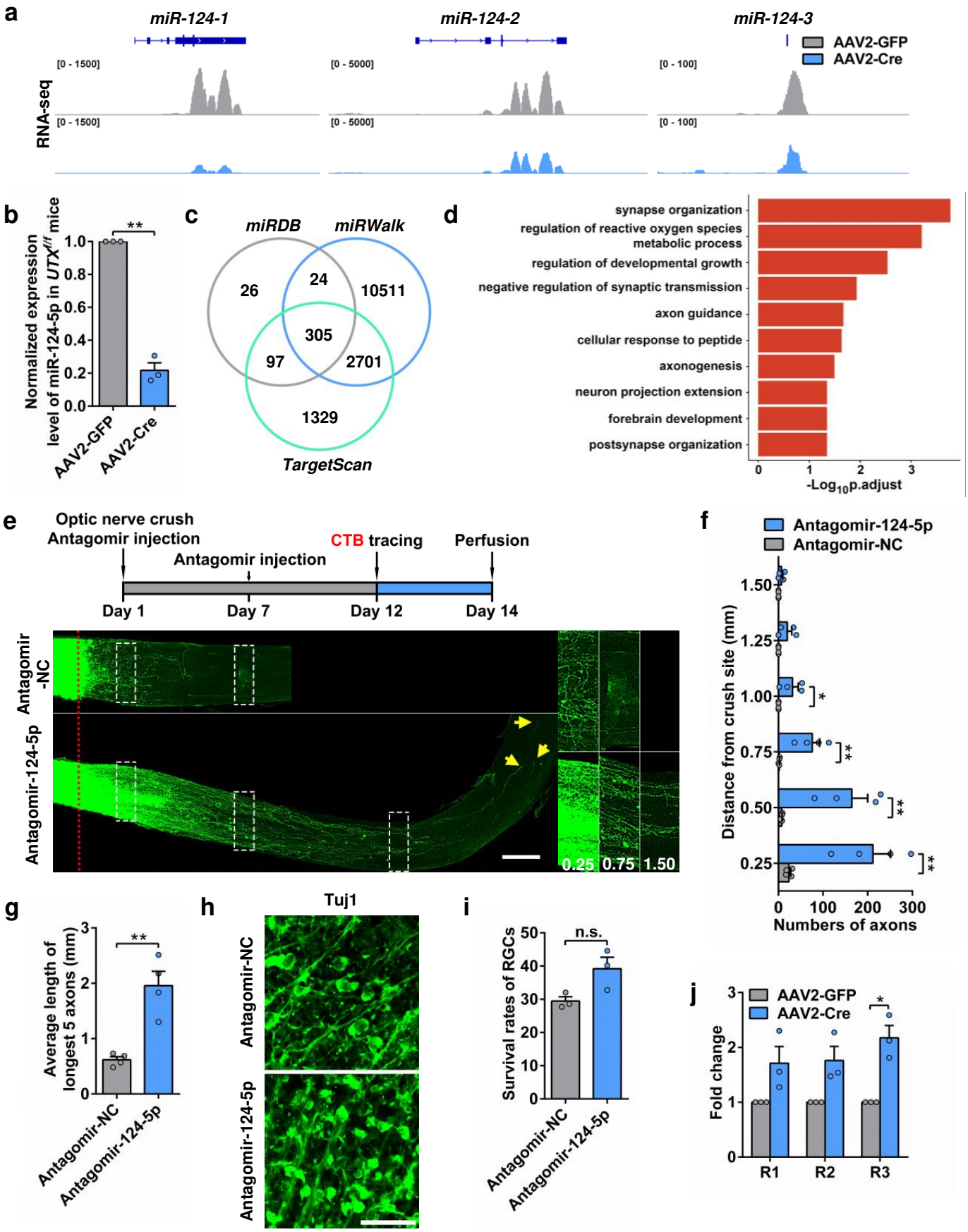
a
miR-124-1
miR-124-2
miR-124-3
AAV2-GFP
AAV2-Cre
RNA-seq
[0 - 1500]
[0 - 5000]
[0 - 100]
b
Normalized expression level of miR-124-5p in UTX f/f mice
AAV2-GFP
AAV2-Cre
c
miRDB
miRWalk
TargetScan
26
24
10511
305
97
2701
1329
d
synapse organization
regulation of reactive oxygen species metabolic process
regulation of developmental growth
negative regulation of synaptic transmission
axon guidance
cellular response to peptide
axonogenesis
neuron projection extension
forebrain development
postsynapse organization
-Log10p.adjust
e
Optic nerve crush
Antagomir injection
Antagomir injection
CTB tracing
Perfusion
Day 1
Day 7
Day 12
Day 14
Antagomir -NC
Antagomir-124-5p
0.25
0.75
1.50
f
Antagomir-124-5p
Antagomir-NC
Distance from crush site (mm)
Numbers of axons
g
Average length of longest 5 axons (mm)
Antagomir-NC
Antagomir-124-5p
h
Tuj1
Antagomir-NC
Antagomir-124-5p
i
Survival rates of RGCs
n.s.
Antagomir-NC
Antagomir-124-5p
j
AAV2-GFP
AAV2-Cre
Fold change
R1
R2
R3

Fig. 7 | Antagomir-mediated inhibition of miR-124-5p significantly boost axon regeneration.

(a) Sample genome tracks showing reduced expression levels of *miR-124-1*(chr14: 64828106-64828190), *miR-124-2*(chr3: 17849826-17849934), and *miR-124-3*(chr2: 180535833-180535900) in the purified RGCs of *UTX*$^{f/f}$ mice injected with AAV2-Cre, compared to *UTX*$^{f/f}$ mice with AAV2-GFP injection. y axis indicates normalized reads.

(b) Real time PCR analysis showing transcription levels of mature antagomir-124-5p in the purified RGCs of *UTX*$^{f/f}$ mice 2 weeks after intravitreal injection of AAV2-GFP or AAV2-Cre, respectively (one sample *t* test, P=0.0034; n=3 independent experiments).

(c) Venn diagram showing overlapped candidate targets of miR-124-5p between three different search engines (miRDB, TargetScan and miRWalk).

(d) Selected Gene Ontology (GO) enrichment for 305 overlapped candidate targets of miR-124-5p (adjusted *P*-value < 0.05).

(e) Top: schematic time course of optic nerve regeneration model. Antagomir was injected immediately after ONC and at day 7 for the second time. Optic nerve regeneration was analyzed 2 weeks after the nerve crush by the fluorescence (Alexa 594) tagged CTB tracing. Bottom: representative 2D projected confocal images of whole mount cleared optic nerves of wild type mice with intravitreal injection of antagomir-NC or antagomir-124-5p 2 weeks after ONC. The regenerating axons were labeled with CTB-Alexa 594. Yellow arrows indicate the distal ends of regenerating axons. The red dotted lines indicate the nerve crush sites. The columns on the right display magnified images of the areas in white, dashed boxes on the left, showing axons at 0.25, 0.75, and 1.50 mm distal to the crush sites. Scale bar, 200 µm for the left column and 100 µm for the magnified images.

(f) Quantification of regenerating axons at different distances distal to the nerve crush site (0.25 to 1.50 mm) in (f) (two tailed student's *t* tests, P<0.05; Antagomir-NC: n=4 mice, Antagomir-124-5p: n=4 mice).

(g) Quantification of the average length of the top 5 longest axons of each nerve in (f) (two tailed student's *t* tests, P=0.0023; Antagomir-NC: n=4 mice, Antagomir-124-5p: n=4 mice).

(h) Fluorescent images of flat whole mount retina immunostained for neuronal marker Tuj1 (green), showing surviving RGCs at 2 weeks after injury. Scale bar, 50 µm.

(i) Quantification of RGC survival rate in (h) (two tailed student's t tests, P=0.0579; Antagomir-NC: n=3 mice, Antagomir-124-5p: n=3 mice). Note that RGC survival rate was higher with antagomir-124-5p injection than with antagomir-NC injection, but the difference was not statistically significant.

(j) The genomic promoter regions (R1-R3) proximal to the *miR-124-2* gene on chromosome 3 (Chr3) were assayed in the chromatin immuno-precipitation (ChIP)-PCR experiment using the antibody against H3K27me3 in the purified RGCs. In the H3K27me3 ChIP-PCR experiment, the genomic region R1, R2, and R3 were amplified from the purified RGCs to bind to H3K27me3.

n.s. $P > 0.05$; *, ** $P < 0.05$, 0.01, respectively. Data are represented as mean ± SEM. See also Extended Data Figs. 12.

Extended Data Figure 1

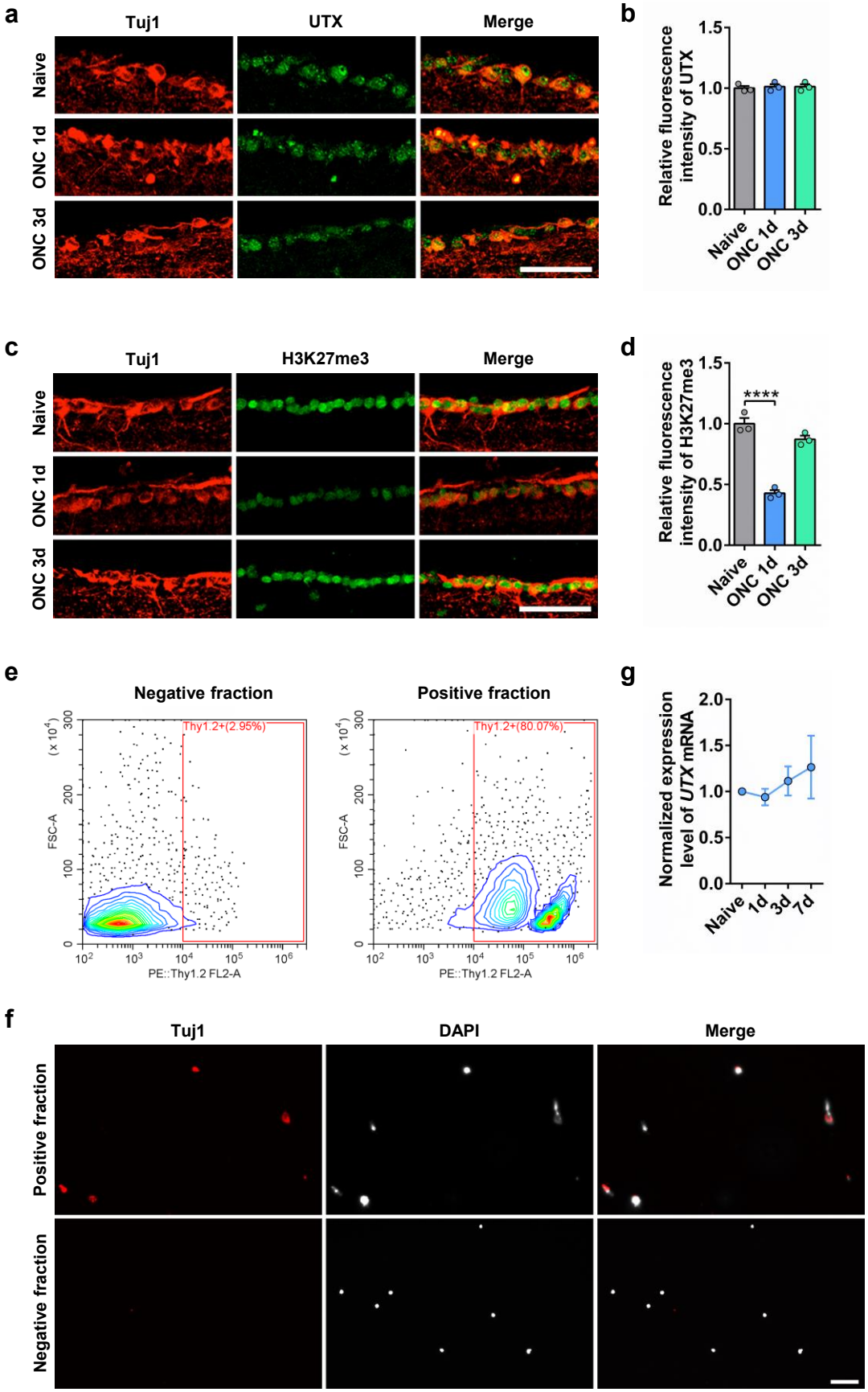

Extended Data Fig. 1 | Changes of UTX or H3K27me3 in retinal ganglion cells (RGCs) after optic nerve crush (ONC), Related to Fig. 2.

(a) Representative images of UTX immunostaining in retina sections showing unchanged level of UTX in RGCs after ONC. Images were stained for neuronal marker Tuj1 (red) and UTX (green). Scare bar, 50 μm.

(b) Quantification of relative fluorescence intensity of UTX immunostaining in (a) (one way ANOVA followed by Tukey's multiple comparison test, P=0.2274; n=3 independent experiments for each condition).

(c) Representative images of H3K27me3 immunostaining in retina sections showing reduced level of H3K27me3 in RGCs after ONC. Images were stained for neuronal marker Tuj1 (red) and H3K27me3 (green). Scare bar, 50 μm.

(d) Quantification of relative fluorescence intensity of H3K27me3 immunostaining in (c) (one way ANOVA followed by Tukey's multiple comparison test, P<0.0001; n=3 independent experiments for each condition).

(e) Positive selection and depletion of Thy1.2+ RGCs by immunomagnetic cell separation (MACS). Labeled retinal cells with anti-mouse Thy1.2 magnetic particles were separated into negative fraction and positive fraction using a magnet. Thy1.2+ cells in each fraction was shown in the right box (red). Flow cytometric analysis showed that the positive rate of Thy1.2 in positive fraction was 80.8±4.43% (n=3 independent experiments). The threshold for Thy1.2+ cells was determined based on the cell distribution in isotype control.

(f) Representative images of Thy1.2+ RGCs after MACS purification. Retinal cells in negative fraction and positive fraction were stained for neuronal marker Tuj1 (red) and DAPI (gray). Scare bar, 50 μm.

(g) Time course of expression of *UTX* transcripts in purified RGCs from naive mice and 1, 3, and 7 days post-optic nerve crush by real time PCR analysis. (one way ANOVA followed by Tukey's multiple comparison test, P=0.6631; n=3 independent experiments for each condition).

****P < 0.0001. Data are represented as mean ± SEM.

Extended Data Figure 2

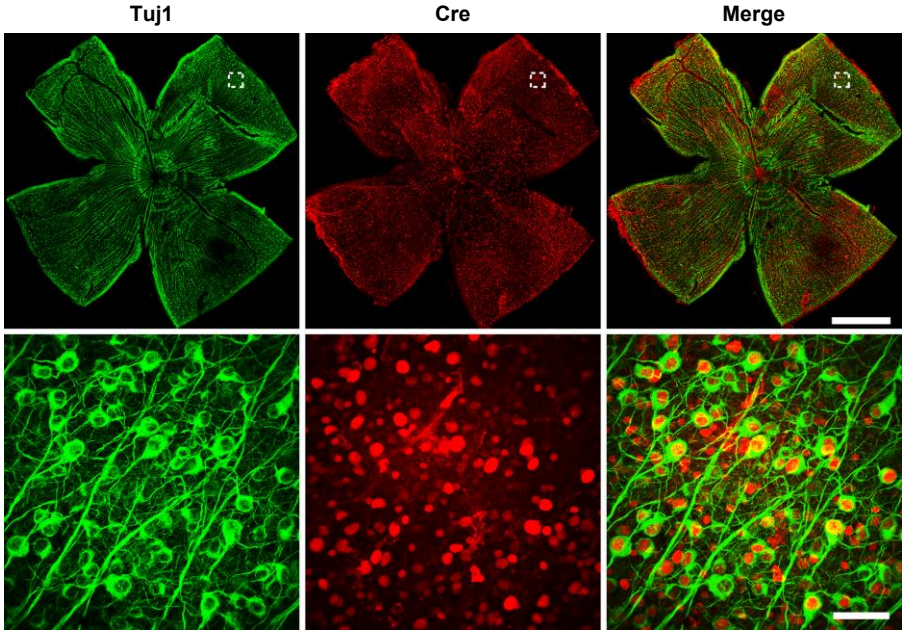

Extended Data Fig. 2 | AAV2-Cre transduction rate in mouse retinal ganglion cells (RGCs), Related to Fig. 2.

Confocal images of flat mounted retinas showing co-immunostaining of Tuj1 (green) and Cre recombinase (red). The bottom row images shows enlarged images of the top row images. The infection rate of AAV2-Cre in RGCs was 88.8±7.56% (n=2 independent experiments). Scale bar, 1 mm in top images and 50 μm in bottom images.

Extended Data Figure 3

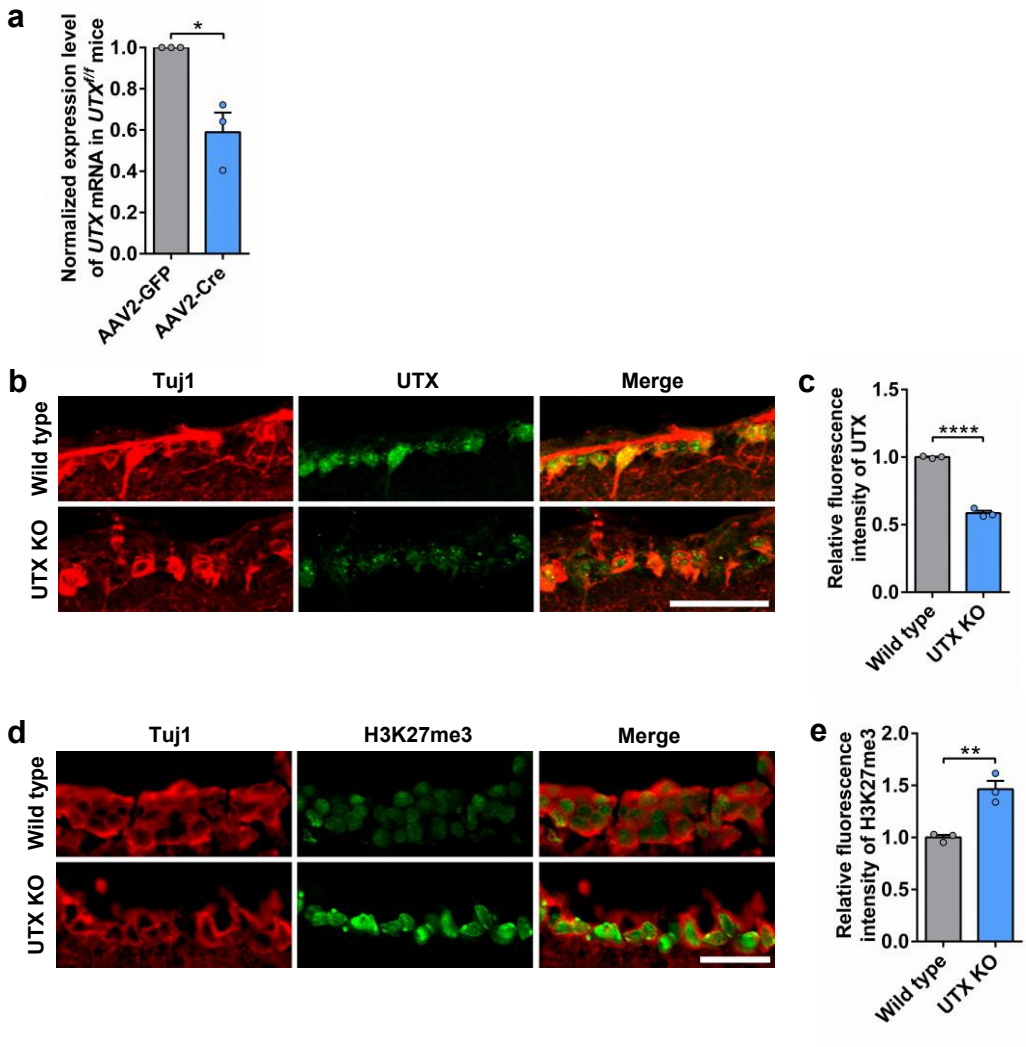

Extended Data Fig. 3 | Deletion of UTX in RGCs triggered significantly increased level of H3K27me3, Related to Fig. 2.

(a) Real time PCR analysis showing mRNA levels of UTX in the purified RGCs of *UTX*$^{f/f}$ mice two weeks after intravitreal injection of AAV2-GFP or AAV2-Cre, respectively (one sample t test, P=0.0499; n=3 independent experiments).

(b) Confocal images of retinal sections showing significantly reduced level of UTX in RGCs of *UTX*$^{f/f}$ mice injected with AAV2-Cre (UTX KO), compared to wild type mice with AAV2-Cre injection (Wild type). The sections were stained for neuronal marker Tuj1 (red), which labeled RGCs, and UTX (green). Scale bar, 50 μm.

(c) Quantification of relative fluorescence intensities of UTX immunostaining shown in (b) (two tailed student's t tests, P<0.0001; n=3 mice for each condition).

(d) Confocal images of retinal sections from wild type and UTX knockout mice (UTX KO) showing markedly increased level of H3K27me3 via deletion of UTX in RGCs. The sections were stained for neuronal marker Tuj1 (red), which labeled RGCs, and H3K27me3 (green). Scale bar, 50 μm.

(e) Quantification of relative fluorescence intensity of H3K27me3 immunostaining shown in (d) (two tailed student's t tests, P=0.0054; n=3 mice for each condition).

*, **,****P < 0.05, 0.01, 0.0001, respectively. Data are represented as mean ± SEM.

Extended Data Figure 4

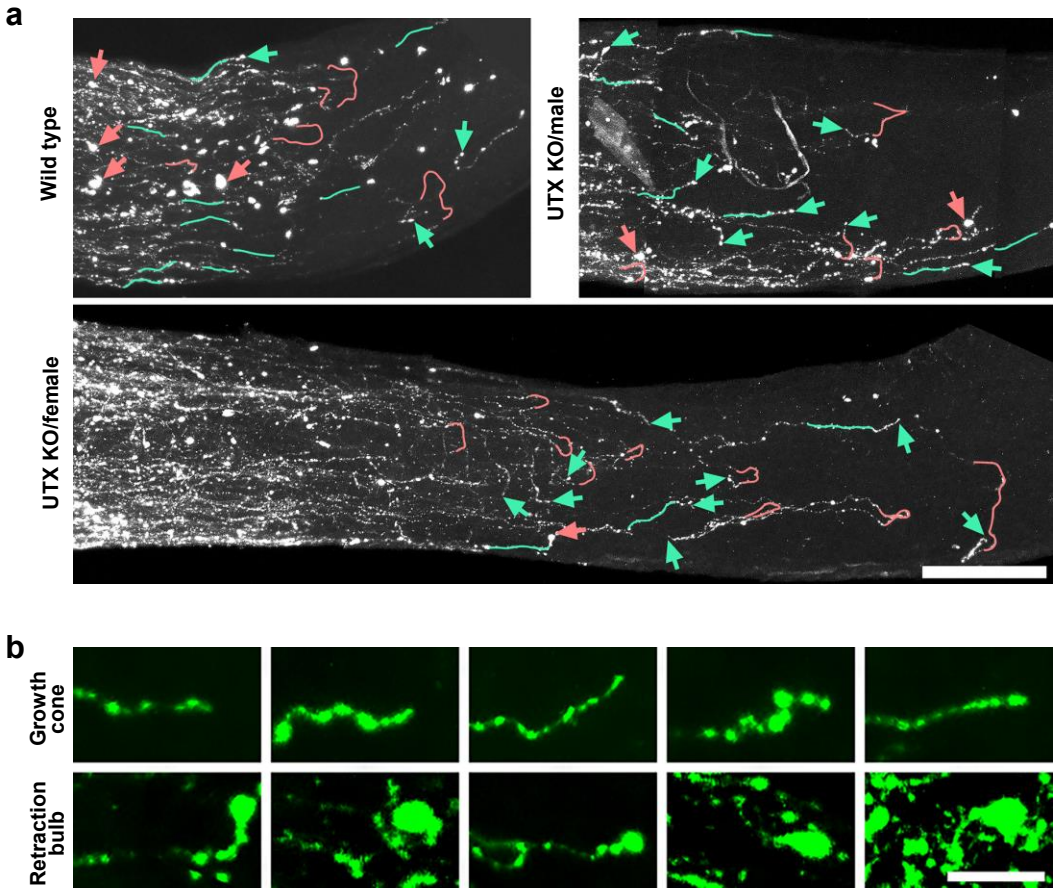

Extended Data Fig. 4 | *UTX* knockout induced changes of axonal morphology, Related to Fig. 2.

(a) Representative images of optic nerves showing that *UTX* deletion modified RGC axonal morphology 2 weeks after ONC. Neurite tracing of single axon showing straight trajectories (green lines) and U-turns (red lines). Red and green arrows indicate retraction bulbs and growth cones, respectively. Scale bar, 200 μm.

(b) Representative images of growth cones and retraction bulbs found in different optic nerves. Scale bar, 25 μm.

Extended Data Figure 5

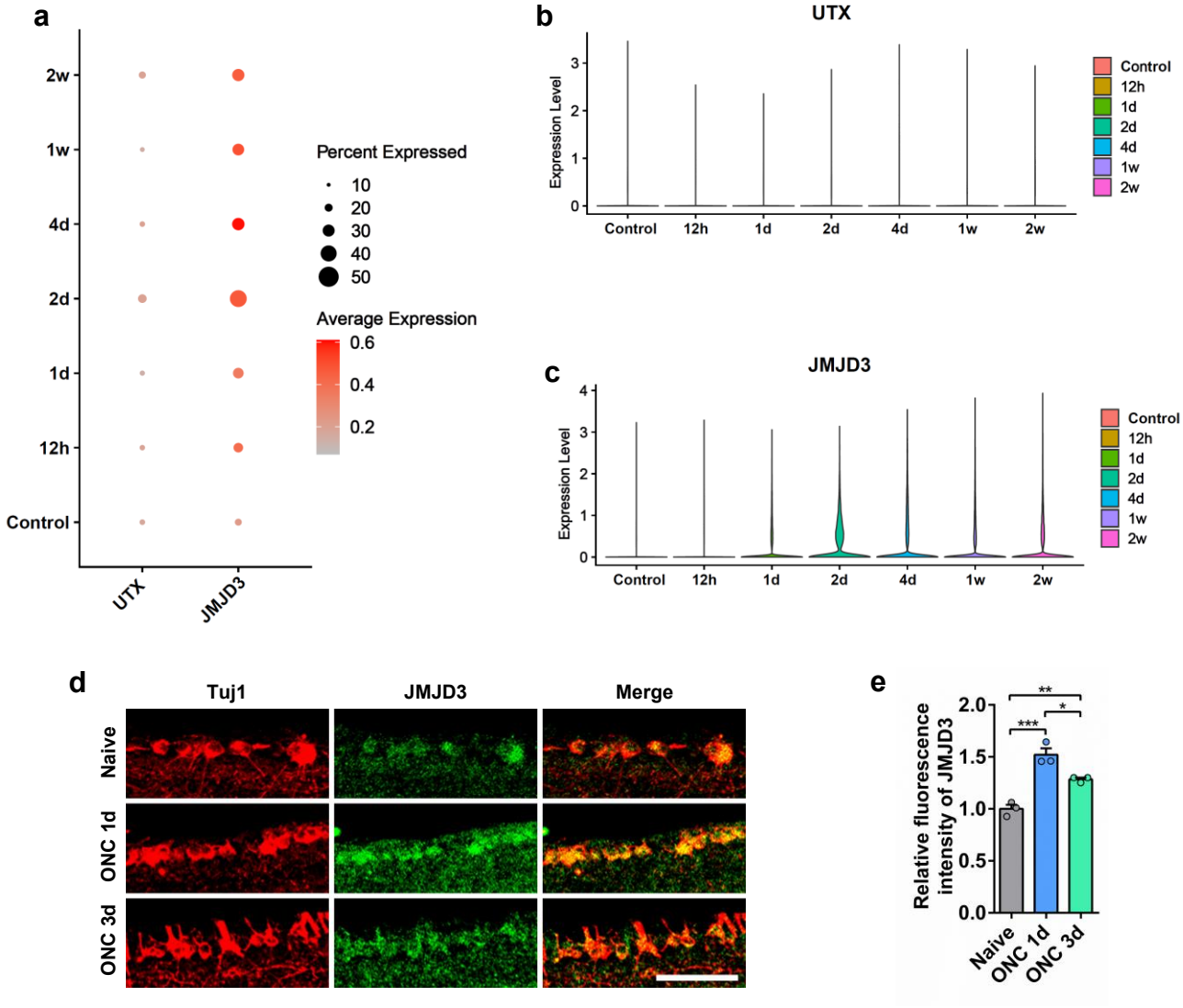

Extended Data Fig. 5 | Changes of JMJD3 or UTX in RGCs after optic nerve crush (ONC), Related to Fig. 2.

(a) Dot plot showing expression patterns of UTX or JMJD3 in RGCs at different time points after ONC. The size of each circle is proportional to the percentage of RGCs expressing UTX or JMJD3 and their intensity depicts the average transcript count within expressing RGCs.

(b) Violin plot indicating the expression distribution of UTX within RGCs at different time points after ONC.

(c) Violin plot indicating the expression distribution of JMJD3 within RGCs at different time points after ONC.

(d) Representative images of JMJD3 immunostaining in retina sections showing unchanged level of JMJD3 in RGCs after ONC. Images were stained for neuronal marker Tuj1 (red) and JMJD3 (green). Scare bar, 50 μm.

(e) Quantification of relative fluorescence intensity of JMJD3 immunostaining in (a) (one way ANOVA followed by Tukey's multiple comparison test, P=0.0004; n=3 independent experiments for each condition).

(a), (b) and (c) obtained from GEO: GSE137398. *, **, ***P < 0.05, 0.01, 0.001, respectively. Data are represented as mean ± SEM.

Extended Data Figure 6

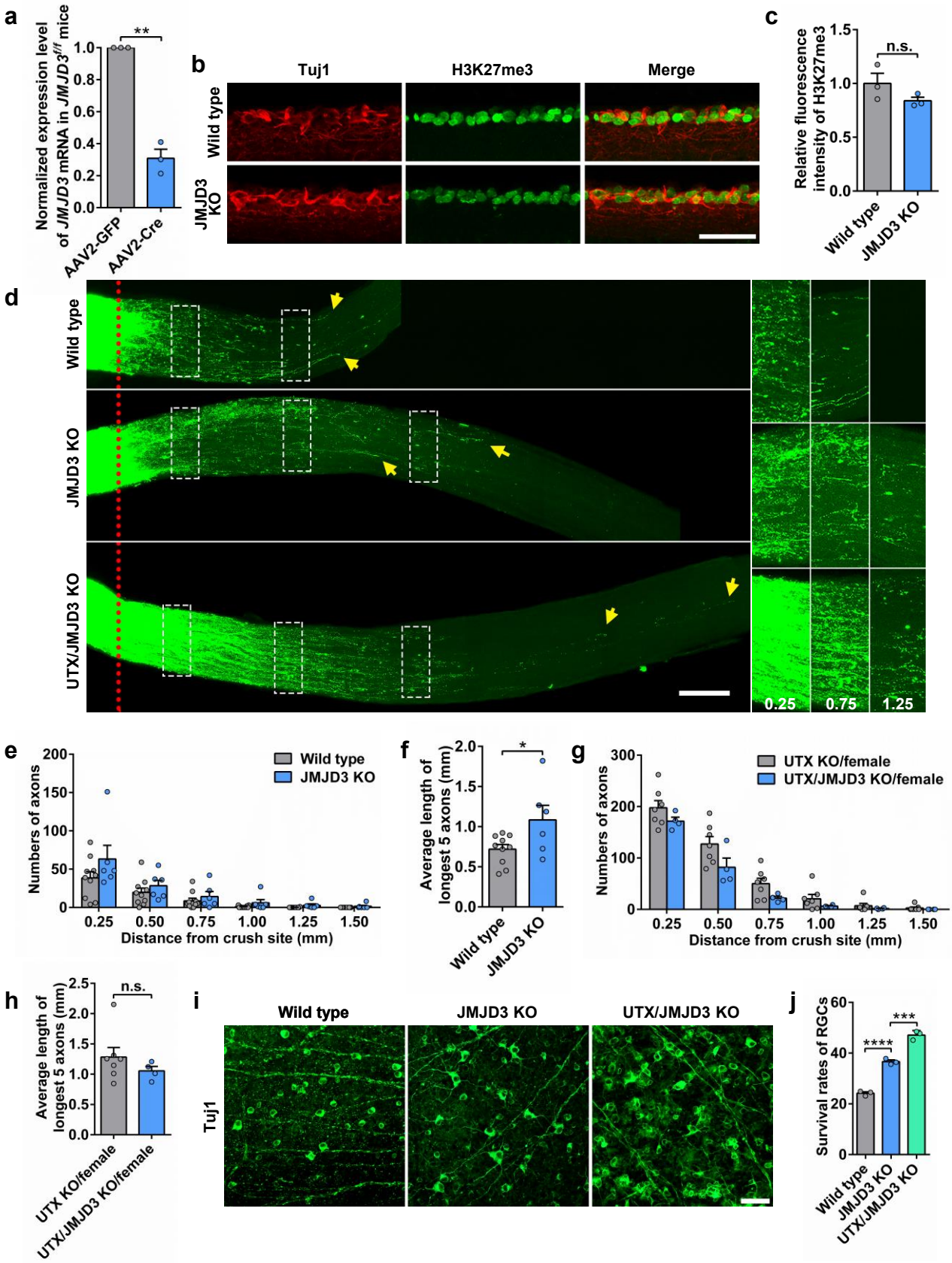

Extended Data Fig. 6 | Knocking out H3K27 demethylase *JMJD3* in mouse retinal ganglion cells (RGCs) markedly enhanced neuronal survival, but poorly promoted axon regeneration, Related to Fig 2.

(a) Real time PCR analysis showing mRNA levels of *JMJD3* in the purified RGCs of *JMJD3*$^{f/f}$ mice two weeks after intravitreal injection of AAV2-GFP or AAV2-Cre, respectively (one sample *t* test, *P*=0.0067; n=3 independent experiments).

(b) Confocal images of retinal sections from wild type and *JMJD3* knockout mice (JMJD3 KO) showing unchanged level of H3K27me3 via deletion of JMJD3 in RGCs. The sections were stained for neuronal marker Tuj1 (red), which labeled RGCs, and H3K27me3 (green). Scale bar, 50 μm.

(c) Quantification of relative fluorescence intensity of H3K27me3 immunostaining shown in (b) (two tailed student's *t* tests, *P*=0.1817; n=3 mice for each condition).

(d) Representative 2D projected confocal images of whole mount cleared optic nerves of wild type, *JMJD3* knockout (JMJD3 KO), *UTX* and *JMJD3* double knockout (UTX/JMJD3 KO) mice 2 weeks after ONC. The regenerating axons were labeled with CTB-Alexa 594. Yellow arrows indicate the distal ends of regenerating axons. The red dotted lines indicate the nerve crush sites. The columns on the right display magnified images of the areas in white, dashed boxes on the left, showing axons at 0.25, 0.75, and 1.25 mm distal to the crush sites. Scale bar, 200 μm for the left column and 100 μm for the magnified images.

(e) Quantification of regenerating axons at different distances distal to the nerve crush site (0.25 to 1.50 mm) in wild type or *JMJD3* knockout mice (JMJD3 KO) after ONC. Bar graph showing no difference in axon regeneration between wild type and JMJD3 KO (two tailed student's *t* tests, *P*>0.05; wild type: n=10 mice, JMJD3 KO: n=6 mice).

(f) Quantification of the average length of the top 5 longest axons of each nerve in wild type or *JMJD3* knockout mice (JMJD3 KO) after ONC (two tailed student's *t* tests, *P*=0.0357; Wild type: n=10 mice, JMJD3 KO: n=6 mice).

(g) Quantification of regenerating axons at different distances distal to the nerve crush site (0.25 to 1.50 mm) in female *UTX* knockout (UTX KO) or female *UTX*/*JMJD3* double knockout mice (UTX/JMJD3 KO) after ONC. Bar graph showing no additive/synergistic effects of *UTX*/*JMJD3* co-deletion on optic nerve regeneration (two tailed student's *t* tests, *P*>0.05; UTX KO: n=7 mice, UTX/JMJD3 KO: n=4 mice).

(h) Quantification of the average length of the top 5 longest axons of each nerve in female *UTX* knockout (UTX KO/female) or female *UTX*/*JMJD3* double knockout mice (UTX/JMJD3 KO/female) after ONC (two tailed student's *t* tests, *P*=0.3282; UTX KO: n=7 mice, UTX/JMJD3 KO: n=4 mice).

(i) Representative images of flat whole mount retina immunostained for neuronal marker Tuj1 (green), indicating increased RGC survival rates in either *JMJD3* knockout (JMJD3 KO) or *UTX*/*JMJD3* double knockout (UTX/JMJD3 KO) mice compared with that in wild type mice. Co-deleting *UTX*/*JMJD3* resulted in additive/synergistic effects on RGC survival. Scale bar, 50 μm.

(j) Quantification of RGC survival rate in (j) (one way ANOVA followed by Tukey's multiple comparisons test, *P*<0.0001; n=3 mice for each condition).

n.s. *P* > 0.05; *, **, ***, ****P < 0.05, 0.01, 0.001, 0.0001, respectively. Data are represented as mean ± SEM.

Extended Data Figure 7

a

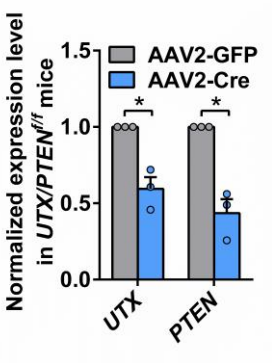

b

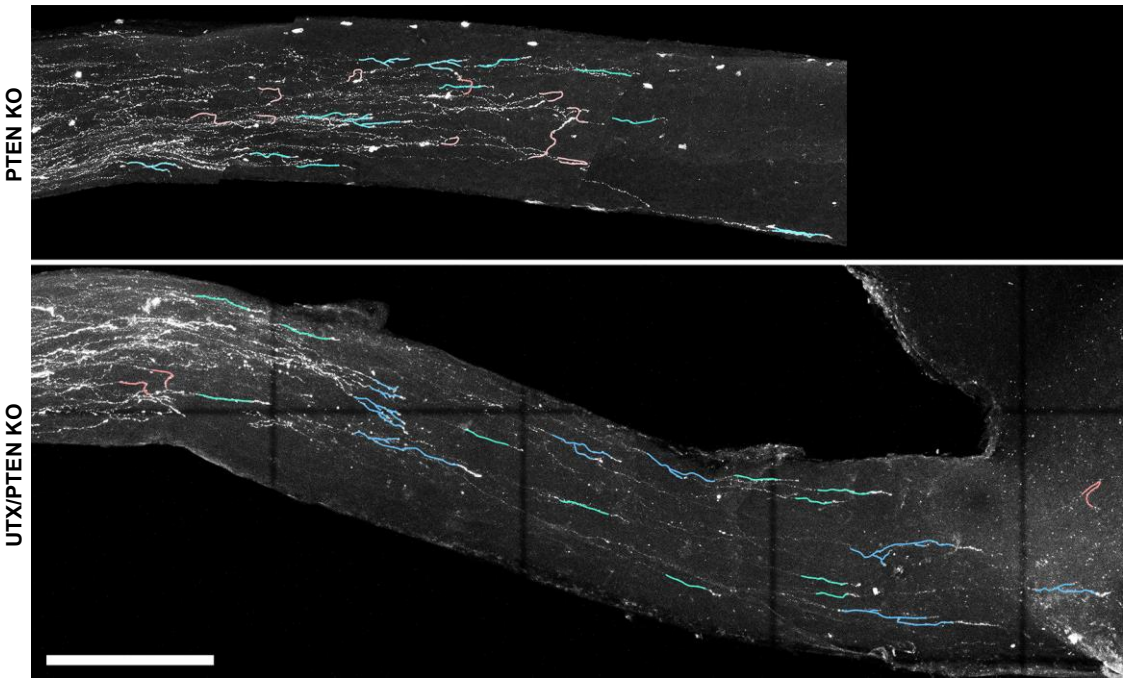

Extended Data Fig. 7 | UTX/PTEN co-deletion significantly decreased U-turns and increased branches, Related to Fig 4.

(a) Real time PCR analyses showing mRNA levels of *UTX* or *PTEN* in the purified RGCs of *UTX/PTEN*$^{f/f}$ mice 2 weeks after intravitreal injection of AAV2-GFP or AAV2-Cre, respectively (one sample *t* test; *UTX*: P=0.0331; *PTEN*: P=0.0253; n=3 independent experiments). $^{*}P < 0.05$. Data are represented as mean ± SEM.

(b) Representative images of U-turns and branches found in the distal nerve region. Neurite tracing showing that co-deletion of *UTX*/*PTEN* in RGCs led to markedly decreased U-turns and increased branches compared to *PTEN* deletion alone. Green lines, red lines and blue lines indicate straight trajectories, U-turns and branches, respectively. Scale bar, 200 μm.

Extended Data Figure 8

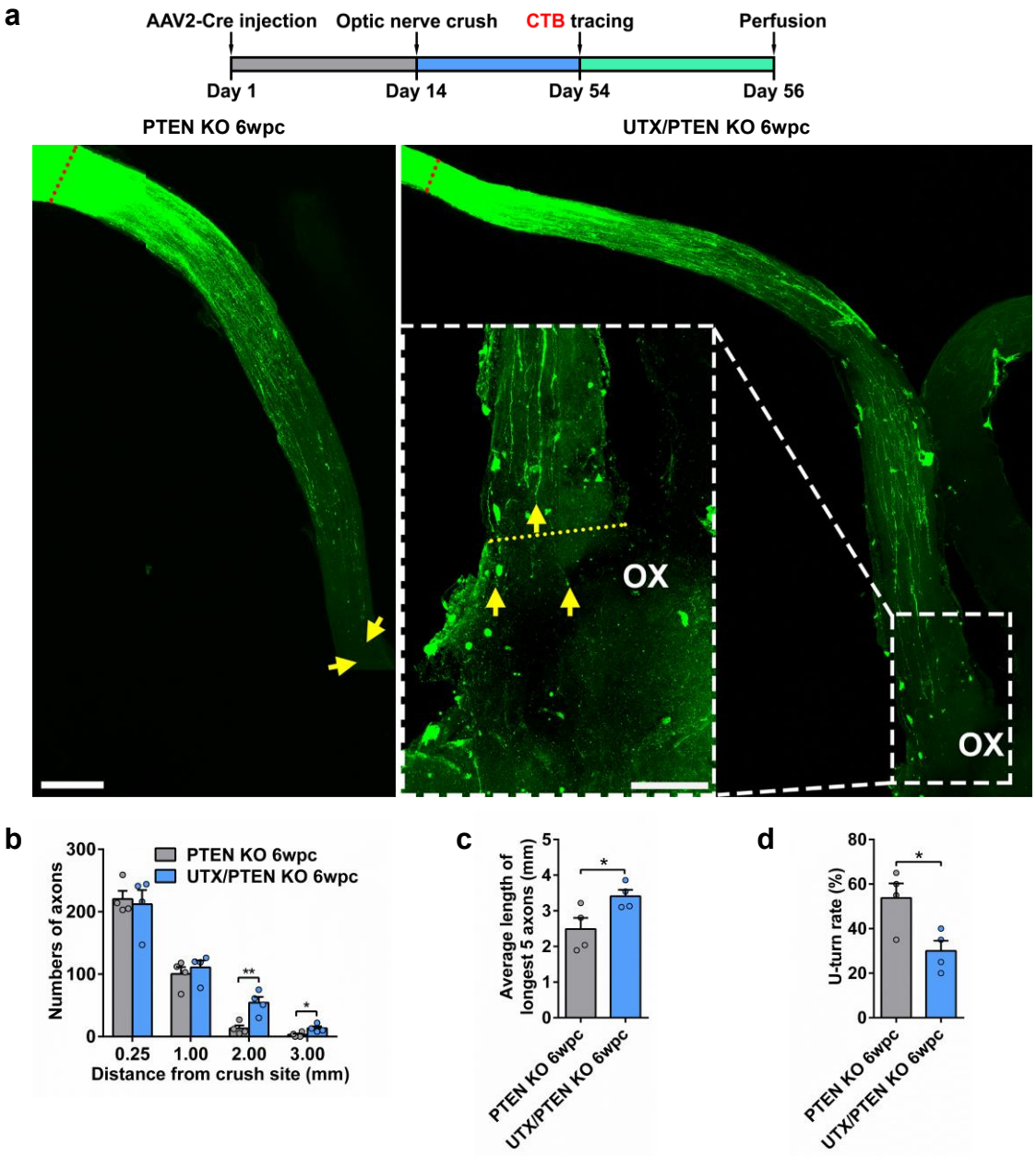

Extended Data Fig. 8 | Synergistic effects of *UTX* and *PTEN* double knockout on axon regeneration observed 6 weeks after ONC, Related to Fig 4.

(a) Top: schematic time course of optic nerve regeneration model. Specifically, AAV2-Cre was injected at day 1 and the optic nerve was crushed 2 weeks later. Optic nerve regeneration was analyzed 6 weeks after the nerve crush, and the fluorescence (Alexa 594) tagged CTB was injected 2 days before collecting the optic nerve. Bottom: representative 2D projected confocal images of whole mount cleared optic nerves of *PTEN* knockout (PTEN KO 6wpc) or *UTX*/*PTEN* double knockout (UTX/PTEN KO 6wpc) mice 6 weeks after ONC. The regenerating axons were labeled with CTB-Alexa 594. The left dashed white box shows enlarged images of areas indicated by the dashed white box on the right. Yellow arrows indicate the distal ends of regenerating axons. Red and yellow dotted lines indicate the nerve crush sites and the optic nerve-chiasm transition zone, respectively. OX indicates the optic chiasm. Scale bar, 200 μm.

(b) Quantification of regenerating axons at different distances distal to the nerve crush site (0.25 to 3.00 mm) in *PTEN* knockout (PTEN KO 6wpc) or *UTX*/*PTEN* double knockout mice (UTX/PTEN KO 6wpc) 6 weeks after ONC (two tailed student's *t* tests, $P<0.05$; PTEN KO 6wpc: n=4 mice, UTX/PTEN KO 6wpc: n=4 mice).

(c) Quantification of the average length of the top 5 longest axons of each nerve in (a) (two tailed student's *t* tests, $P=0.0442$; PTEN KO 6wpc: n=4 mice, UTX/PTEN KO 6wpc: n=4 mice).

(d) Quantification of U-turn rate in (a) (two tailed student's *t* tests, $P=0.0250$; PTEN KO 6wpc: n=4 mice, UTX/PTEN KO 6wpc: n=4 mice; top 20 longest axons were analyzed for each mouse).

*, **$P < 0.05$, 0.01, respectively. Data are represented as mean ± SEM.

Extended Data Figure 9

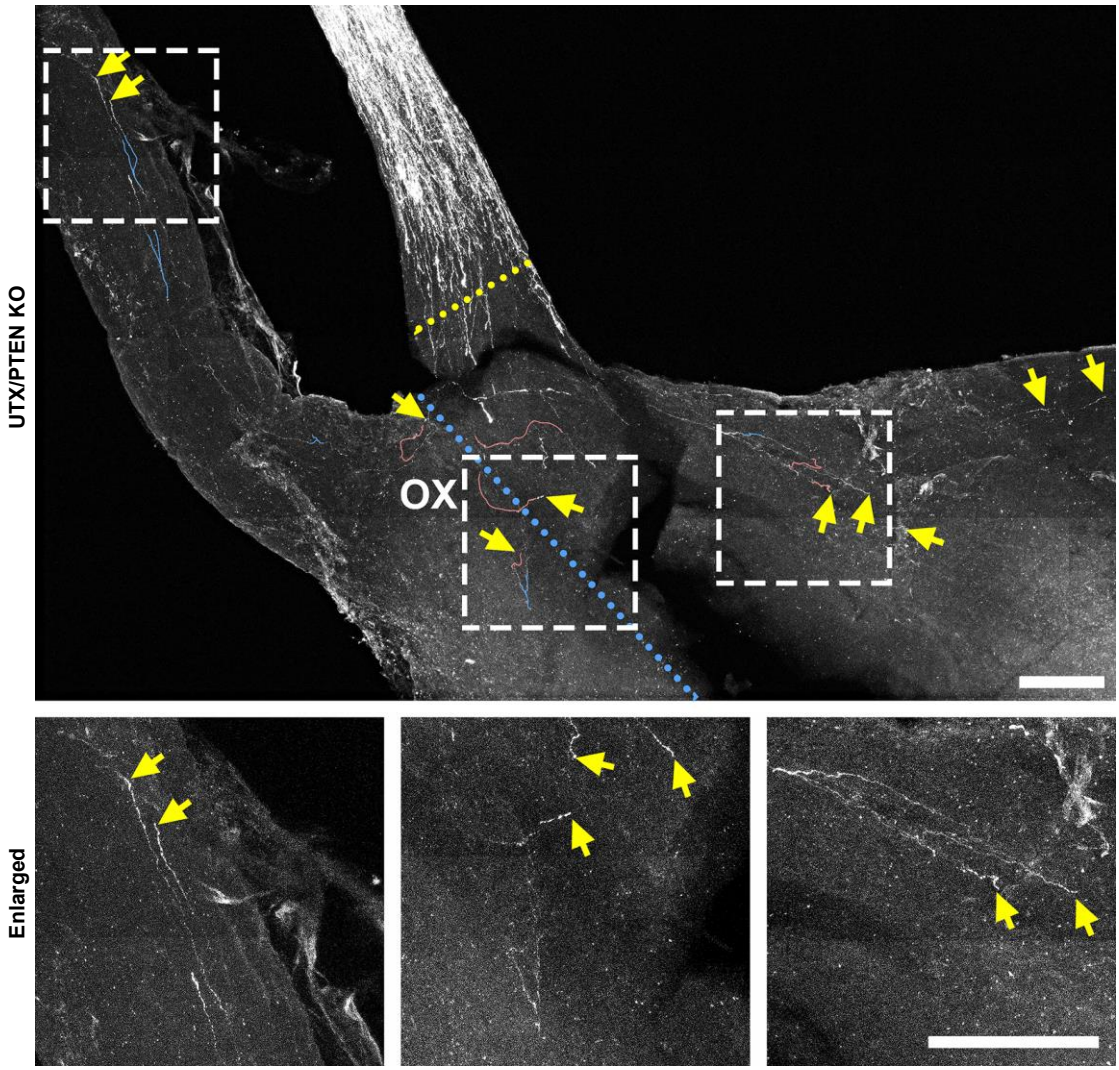

Extended Data Fig. 9 | Regenerating axons into the optic chiasm shows complex growth patterns in *UTX*/*PTEN* double knockout mice, Related to Fig 4.

Neurite tracing of regenerating axon into the optic chiasm showing complex growth patterns in *UTX*/*PTEN* double knockout mice. The bottom row shows enlarged images of areas indicated by the dashed white boxes in the top row. The regenerating axons at the optic chiasm were labeled with CTB-Alexa 594. Yellow arrows indicate the distal ends of regenerating axons. Blue and yellow dotted lines indicate the chiasm midline and the optic nerve-chiasm transition zone, respectively. Green lines, red lines and blue lines indicate straight trajectories, U-turns and branches, respectively. OX indicates the optic chiasm. Scale bar, 200 μm.

Extended Data Figure 10

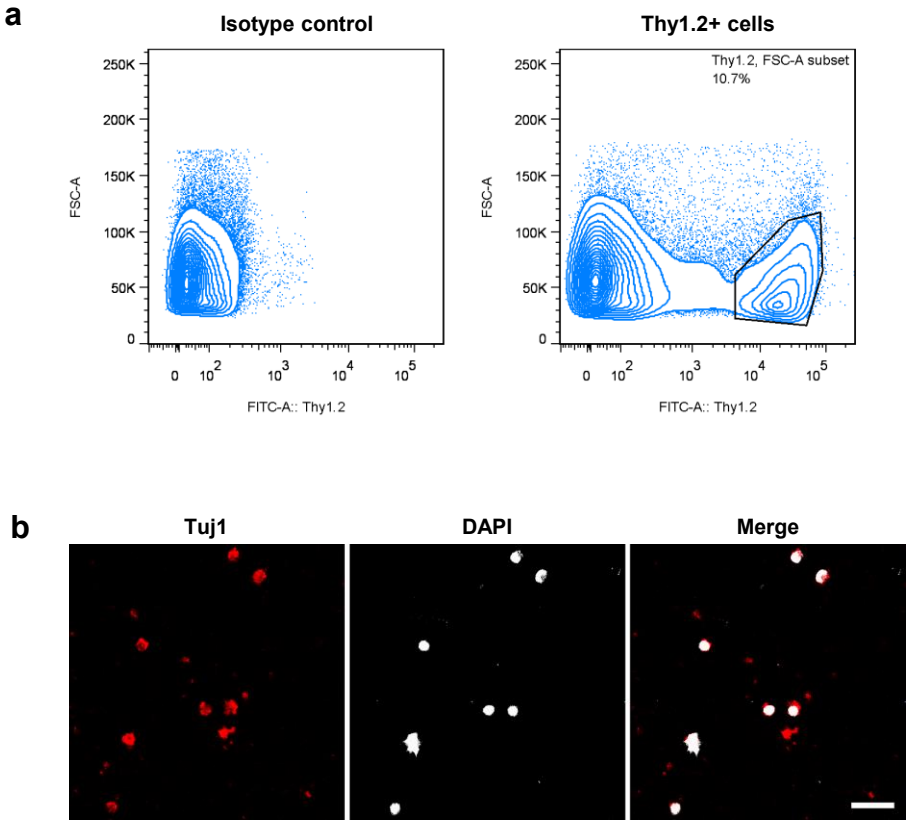

Extended Data Fig. 10 | Enrichment of mouse Thy1.2+ RGCs by fluorescence-activated cell sorting (FACS) for high throughput sequencing, Related to Fig 5, 6.

(a) Representative FACS plots showing RGCs enrichment. Retinal cells labeled with isotype antibody were used as controls to set up the threshold for Thy1.2+ cells. Thy1.2+ RGCs were collected according to isotype control. Cell viability was determined with DAPI staining.

(b) Representative images of Thy1.2+ RGCs after FACS sorting. Purified RGCs were stained for neuronal marker Tuj1 (red) and DAPI (gray). Scare bar, 20 μm.

Extended Data Figure 11

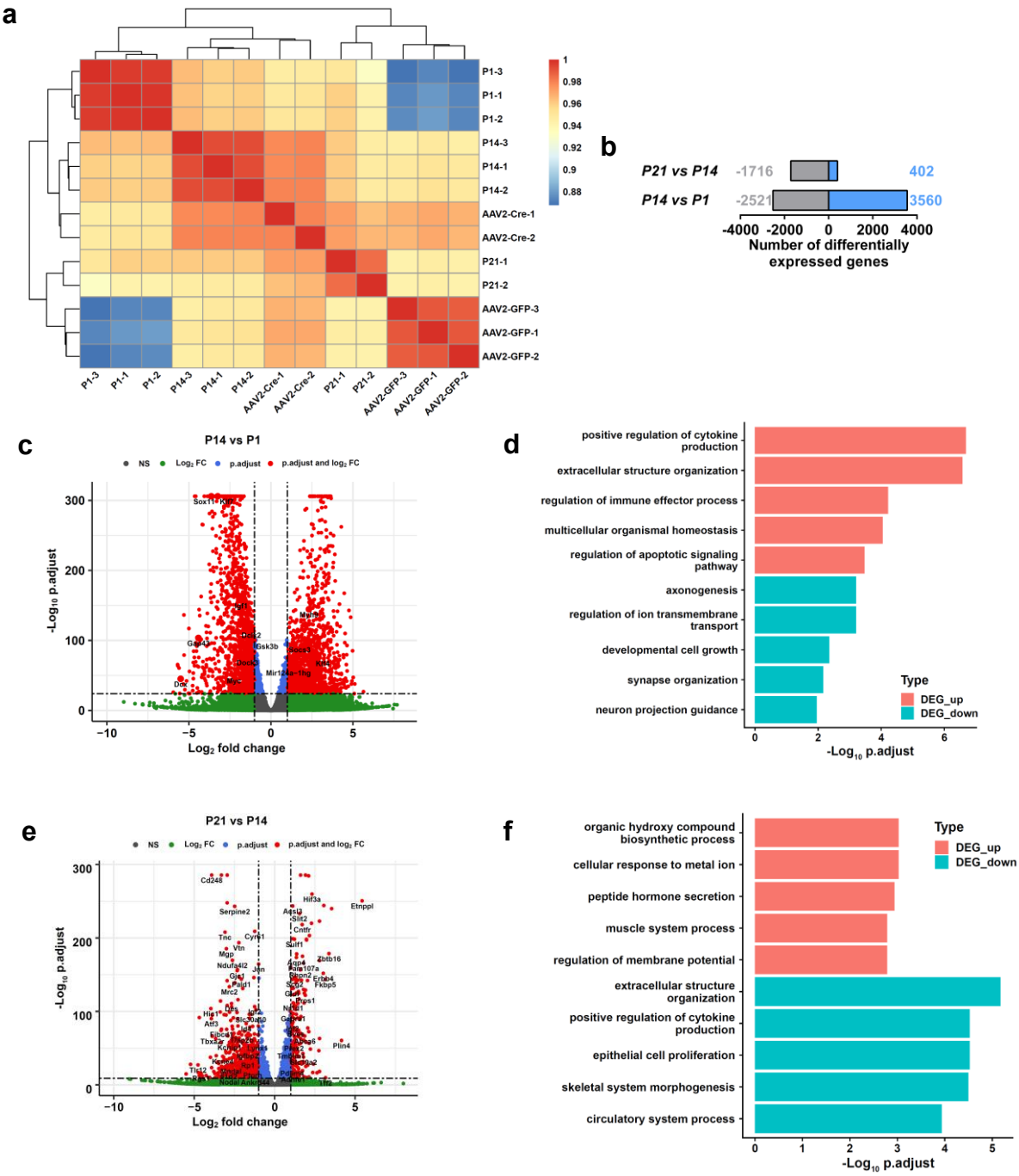

Extended Data Fig. 11 | Axon growth competence reduces during neuronal maturation, Related to Fig 5, 6.

(a) Pearson's correlation analysis of normalized expression levels of all biological samples, including different developmental stages (P1, P14 and P21), 3 days post-injury RGCs from wild type (AAV2-GFP) and UTX KO (AAV2-Cre) mice.

(b) Number of differentially expressed genes during neuronal maturation at the threshold of adjusted *P*-value < 0.05.

(c) Volcano plot showing differential gene expression between P14 and P1 RGCs. Positive $\log_2$ fold change indicates higher expression in P14 RGCs relative to P1 RGCs. Red points indicate that genes are considered significantly different if absolute $\log_2$ Fold change > 1 and adjusted *P*-value < 0.05; vertical and horizontal reference lines at respective values.

(d) Top 5 gene ontology (GO) terms were generated separately for genes upregulated or downregulated (adjusted *P*-value < 0.05) by P14 RGCs relative to P1 RGCs.

(e) Volcano plot showing differential gene expression between P21 and P14 RGCs. Positive $\log_2$ fold change indicates higher expression in P21 RGCs relative to P14 RGCs. Red points indicate that genes are considered significantly different if absolute $\log_2$ Fold change > 1 and adjusted P-value < 0.05; vertical and horizontal reference lines at respective values.

(f) Top 5 gene ontology (GO) terms were generated separately for genes upregulated or downregulated (adjusted *P*-value < 0.05) by P21 RGCs relative to P14 RGCs.

Extended Data Figure 12

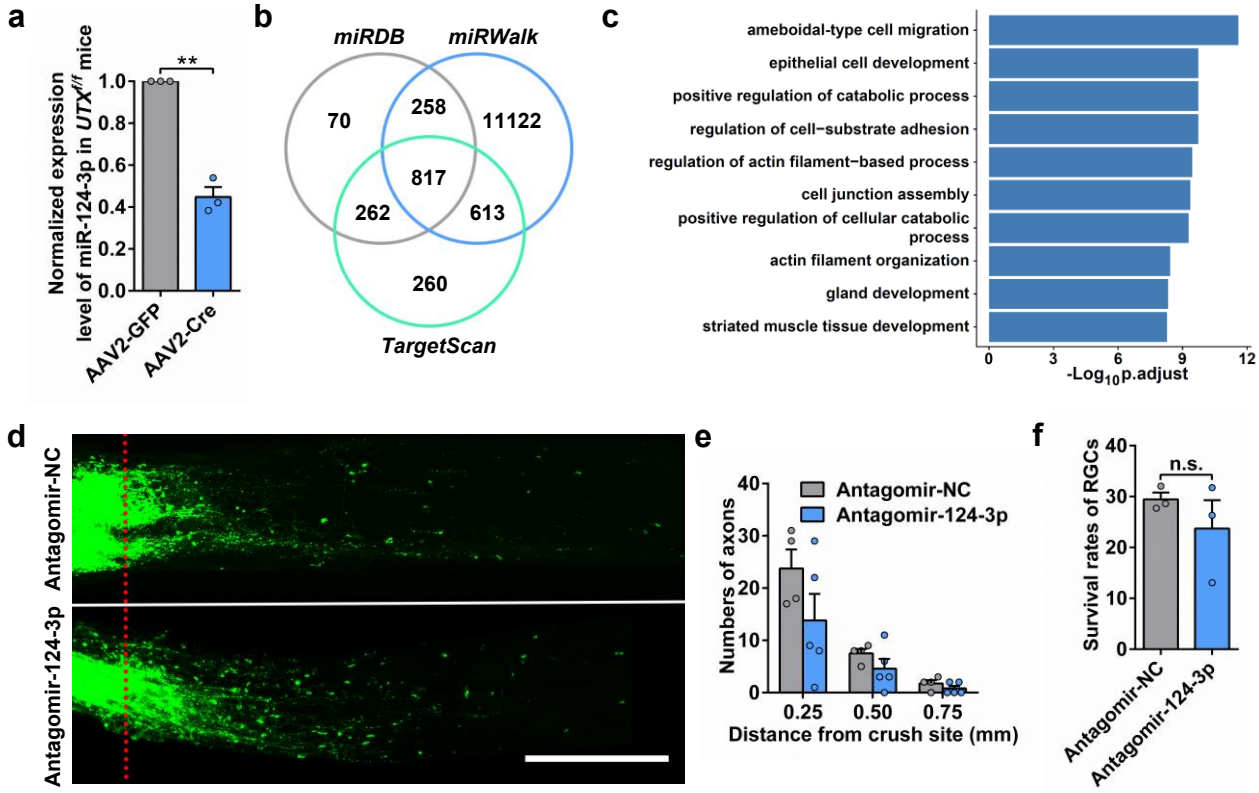

Extended Data Fig. 12 | No effect of antagomir-124-3p on RGC survival and optic nerve regeneration, Related to Fig 7.

(a) Real time PCR analysis showing transcription levels of mature antagomir-124-3p in the purified RGCs of *UTX*$^{f/f}$ mice 2 weeks after intravitreal injection of AAV2-GFP or AAV2-Cre, respectively (one sample *t* test, *P*=0.0072; n=3 independent experiments).

(b) Venn diagram showing overlapped candidate targets of miR-124-3p between three different search engines (miRDB, TargetScan and miRWalk).

(c) Top 10 enriched GO terms of 817 overlapped candidate targets of miR-124-3p (adjusted *P*-value < 0.05).

(d) Representative 2D projected confocal images of whole mount cleared optic nerves of wild type mice injected with antagomir-NC or antagomir-124-3p 2 weeks after ONC. The regenerating axons were labeled with CTB-Alexa 594. The green dotted lines indicate the nerve crush sites. Scale bar, 200 μm.

(e) Quantification of regenerating axons at different distances distal to the nerve crush site (0.25 to 0.75 mm) in (b). Bar graph showing no difference in axon regeneration between antagomir-NC and antagomir-124-3p (two tailed student's *t* tests, *P* > 0.05; antagomir-NC: n=4 mice, antagomir-124-3p: n=5 mice).

(f) Quantification of RGC survival as measured by Tuj1 staining (two tailed student's *t* tests, *P*=0.3711; n=3 mice for each condition). Note no effect of miR-124-3p inhibition on RGC survival.

n.s. *P* > 0.05. Data are represented as mean ± SEM.